



# Joint Action and Competition between Centrifugal, Magnetorotational, and Magnetic Buoyancy Instabilities

M. J. Gradzki<sup>1</sup> , D. W. Hughes<sup>2</sup> , and K. A. Mizerski<sup>1</sup> 

<sup>1</sup>Department of Magnetism, Institute of Geophysics, Polish Academy of Sciences, ul. Ksiecia Janusza 64, 01-452, Warsaw, Poland; [mgradzki@igf.edu.pl](mailto:mgradzki@igf.edu.pl)

<sup>2</sup>School of Mathematics, University of Leeds, Leeds LS2 9JT, UK

Received 2022 December 25; revised 2023 March 29; accepted 2023 April 3; published 2023 August 10

## Abstract

Instabilities driven by some combination of rotation, velocity shear, and magnetic field in a stratified fluid under gravity play an important role in many astrophysical settings. Of particular note are the centrifugal instability, the magnetorotational instability, and magnetic buoyancy instability. Here, we consider a Cartesian model of an equatorial region incorporating all the physical ingredients necessary to study their competition. We investigate the linear instability to interchange (“axisymmetric”) modes of an inviscid, perfectly conducting, isothermal gas, including the effects of rotation, velocity shear, and poloidal and toroidal magnetic fields. The stability problem can be reduced to a second-order boundary value problem, with the growth rate as the eigenvalue. We can make analytic progress through consideration of the physically relevant regime in which the transverse horizontal wavenumber  $k \gg 1$ . Via a perturbation analysis, with  $1/k$  as the small parameter, we can derive the growth rate and the spatial dependence of the eigenfunctions: the unstable modes are strongly localized in the vertical direction, being either *wall modes* (localized near a boundary of the domain) or *body modes* (localized in the interior). We describe the conditions under which the joint action of the separate instability mechanisms leads to enhancement or suppression of the instability. Our analytical results are supplemented by numerical solutions of the stability problem. The most unstable mode found analytically is typically in excellent agreement with that found numerically through consideration of a wide range of wavenumbers. Finally, we discuss how our results relate to the solar tachocline.

*Unified Astronomy Thesaurus concepts:* [Magnetohydrodynamics \(1964\)](#); [Solar magnetic fields \(1503\)](#); [Perturbation methods \(1215\)](#)

## 1. Introduction

Differential rotation, magnetic fields, and convective stratification—stable or unstable—are crucial ingredients in determining the dynamics of all astrophysical bodies. Understanding the instabilities that may arise from these various elements is thus an important goal in astrophysical fluid dynamics. In its simplest form, in which the effects of magnetic field, stratification, and diffusion are all neglected, a differential rotation profile is unstable if, somewhere, the angular momentum decreases with cylindrical radius, a result that dates back to Rayleigh (1917). The criterion for this centrifugal instability (CI) is modified by the incorporation of magnetic fields and convective stratification, as shown by Acheson (1978). Of great astrophysical interest is that a weak magnetic field can destabilize a flow that is stable by the Rayleigh criterion (i.e., a flow with angular momentum everywhere decreasing outwards). This instability, now known as the magnetorotational instability (MRI), was first investigated by Velikhov (1959), Chandrasekhar (1960) and later by Acheson (1978). However, its tremendous astrophysical significance, as an instability mechanism capable of destabilizing Keplerian flows, as occur in accretion disks, was not recognised until the work of Balbus & Hawley (1991). Subsequent to this extremely important realization, there has been a huge amount of research into the MRI: in the linear and nonlinear regimes,

computationally and experimentally, and with a variety of magnetic field configurations (see, e.g., Hawley et al. 1995; Balbus & Hawley 1998; Goodman & Ji 2002; Balbus 2003; Hollerbach & Rüdiger 2005; Ogilvie 2007; Fromang et al. 2013).

A horizontal magnetic field that varies with depth can also act as the agent for destabilizing a convectively stable atmosphere through the mechanism known as magnetic buoyancy instability (MBI). MBI was first analyzed, via the energy principle and in a general setting, by Newcomb (1961); it was first investigated in an astrophysical context by Parker (1966), who proposed MBI as the mechanism for the clumping of the interstellar medium. Subsequently, MBI has been invoked as the dominant mechanism underlying the escape of magnetic field from the solar tachocline, as reviewed by Hughes (2007), and can also be an important player in the dynamics of accretion disks (e.g., Foglizzo & Tagger 1994). Theoretical developments of MBI have been undertaken both in the linear regime (e.g., Gilman 1970; Acheson 1978, 1979; Hughes 1985) and through numerical simulations of the nonlinear development of the instability (e.g., Cattaneo & Hughes 1988; Matthews et al. 1995; Kim et al. 1998; Fan 2001; Kersalé et al. 2007; Hughes & Brummell 2021).

Although studies of CI, MRI, or MBI most often treat the instability mechanisms in isolation, astrophysical bodies, in general, possess regions of differentially rotating, convectively stratified, magnetized fluid; the solar tachocline, for example, is clearly a magnetized region of strong differential rotation. It is thus important to consider the competition between these various instabilities. Our aim therefore in this paper is to consider a framework in which we can analyze this



Original content from this work may be used under the terms of the [Creative Commons Attribution 4.0 licence](#). Any further distribution of this work must maintain attribution to the author(s) and the title of the work, journal citation and DOI.

competition. We consider a local Cartesian model, similar to that of the shearing box approximation, involving all the necessary factors for development of CI or MRI, and MBI. The domain is a local representation of the equatorial region, with the rotation axis perpendicular to gravity. As a basic state, we include the effect of velocity shear—a horizontal (“toroidal”) flow, perpendicular to rotation and dependent on height—a constant “poloidal” magnetic field (parallel to the rotation axis) and a toroidal field of strength decreasing with height. We perform a linear stability analysis, making the simplifying assumption that all perturbation quantities are “axisymmetric.” The key feature is applying a Rayleigh–Schrödinger perturbation analysis in the limit of short-horizontal-wavelength perturbations, where “short” is in comparison with the vertical variation of basic-state quantities such as density or pressure. The short-horizontal-wavelength assumption has the consequence that the perturbations become highly localized vertically. Thus, through a boundary and/or internal layer analysis, following the approach adopted in Mizerski et al. (2013), Bowker (2016), and Gradzki & Mizerski (2018), we are able to determine a height-dependent growth rate function  $\sigma(z)$  and hence determine the location of the localization of the eigenfunctions. As explained in Bowker (2016), the presence of strong shear is a complicating feature of the analysis: in particular, the relation between the particular growth rate value  $\sigma(z_0)$  at a selected height  $z_0$  and the height at which the eigenmode associated with this eigenvalue is localized becomes highly nonobvious. We are able to compare our asymptotic solutions with solutions of the full system obtained numerically. Our work should be regarded as being complementary to earlier studies by Acheson (1978) and Gilman (2018a, 2018b), both of whom also explored systems in which CI, *azimuthal* MRI, and MBI could occur. Acheson (1978) performed a local linear stability analysis, in cylindrical geometry, of a quite general system involving basic-state functions that depend on both radius  $r$  and axial direction  $z$ , making analytic progress with this complicated system through the consideration of specific asymptotic parameter regimes. Gilman (2018a, 2018b) also performed a local stability analysis, in spherical geometry, of basic states with only toroidal flows and toroidal magnetic fields, focusing particularly on profiles appropriate to the solar tachocline. He found that for solar-type differential rotation, at low latitudes, the azimuthal wavenumber  $m$  of the most unstable perturbations in the absence of poloidal magnetic field is a function of latitude and the strength of the toroidal field; however, for toroidal fields as strong as  $\sim 20$  kG, the MBI instability became dominant, with the most unstable mode being that with  $m=0$ —see Figure 6 in Gilman (2018b). In contrast to Acheson (1978) and Gilman (2018a, 2018b), our basic-state magnetic field has a (uniform) poloidal component, which is necessary for bringing the axisymmetric MRI into play. In this sense, although we are neglecting nonaxisymmetric perturbations, thus removing the azimuthal MRI, we can study the coupling between the axisymmetric MRI (i.e., its standard version, triggered by poloidal field) and the MBI, which to our knowledge has not hitherto been investigated, either numerically or analytically.

The paper is organized as follows. The mathematical formulation of the problem is contained in Section 2. Sections 3 and 4 contain, respectively, the main results of the leading and first-order asymptotic analyses for the growth rate

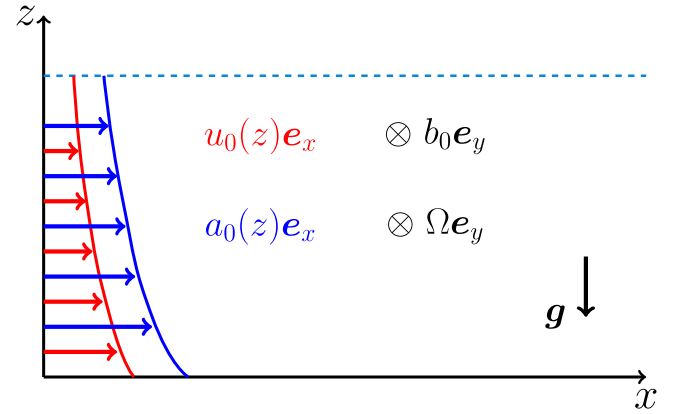


**Figure 1.** Configuration of the basic state, with depth-dependent horizontal shear flow  $u_0(z)$ , depth-dependent toroidal field  $a_0(z)$ , constant poloidal field  $b_0$ , rotation  $\Omega$  and gravity  $g$ .

$\sigma$ ; the details of the calculations can be found in Appendix C (leading order) and Appendix D (higher order). Section 5 presents the numerical solutions of the full linear stability equations for some selected representative parameter values, and makes a comparison with those obtained via the short-horizontal-wavelength perturbation approach. In Section 6, we summarize and discuss the results.

## 2. Mathematical Formulation

Following Gilman (1970) and Mizerski et al. (2013), we consider a plane layer, of thickness  $d$ , of compressible, inviscid, isothermal, and electrically perfectly conducting fluid, described by the perfect gas equation of state. The geometry of the system corresponds to that of the local shearing box approximation, often applied locally to natural systems such as accretion discs, or stellar and planetary interiors at the equator (e.g., Hawley et al. 1995). We adopt a Cartesian coordinate system in which the  $x$ -axis points east (the “toroidal” direction), the  $y$ -axis north, and the  $z$ -axis radially (in the direction opposite to gravity). We assume the presence of a constant acceleration of effective gravity  $\mathbf{g} = (0, 0, -g)$ , and constant rotation  $\Omega = (0, \Omega, 0)$ . The basic state is characterized by a depth-dependent toroidal shear flow  $\mathbf{u}_0(z) = (u_0(z), 0, 0)$  and a magnetic field with depth-dependent, toroidal component and constant poloidal component,  $\mathbf{B}_0(z) = (a_0(z), b_0, 0)$  (see Figure 1). Such a physical setting is constructed in order to accommodate three types of linear instability—MBI, MRI, and CI—and to study the interactions and competition between them.

The system of equations for the velocity  $\mathbf{u}$ , the magnetic field  $\mathbf{B}$ , density  $\rho$ , and pressure  $p$ , consists of the Navier–Stokes (momentum) equation, the mass conservation (continuity) equation, the magnetic induction equation (supplemented by the solenoidal condition on the magnetic field), and the equation of state of an ideal gas. For the purpose of nondimensionalization, we adopt the layer thickness  $d$  and the freefall time  $\sqrt{d/g}$  for the units of length and time respectively. For the units of velocity in the  $y$ - and  $z$ -directions, we choose the freefall velocity  $\sqrt{gd}$ ; however, for the  $x$ -component, we adopt a typical magnitude of the shear flow  $U_s$ . We denote the scales of pressure, density, and magnetic field by  $p_s, \rho_s, B_s$  respectively, where  $p_s$  and  $\rho_s$  are taken as the values of pressure and density at the top of the layer. In dimensionless form, the governing

equations may be expressed as

$$\rho \frac{\partial \mathbf{u}}{\partial t} + \mathcal{U}_\Omega \rho \mathbf{e}_z \times \mathbf{u} + \rho \mathbf{u} \cdot \nabla \mathbf{u} = -\nabla \left( \mathcal{P}p + \Lambda \frac{\mathbf{B}^2}{2} \right) + \Lambda \mathbf{B} \cdot \nabla \mathbf{B} - \rho \mathbf{e}_z, \quad (1)$$

$$\frac{\partial \rho}{\partial t} + \nabla \cdot (\rho \mathbf{u}) = 0, \quad (2)$$

$$\frac{\partial \mathbf{B}}{\partial t} + \mathbf{u} \cdot \nabla \mathbf{B} = \mathbf{B} \cdot \nabla \mathbf{u} - \mathbf{B}(\nabla \cdot \mathbf{u}), \quad (3)$$

$$\nabla \cdot \mathbf{B} = 0, \quad (4)$$

$$p = \alpha \rho. \quad (5)$$

The (positive) nondimensional parameters are defined as

$$\mathcal{U}_\Omega = \frac{2\Omega d}{\sqrt{gd}}, \quad \mathcal{P} = \frac{p_s}{\rho_s g d}, \quad \Lambda = \frac{B_s^2}{\mu_0 \rho_s g d} = \beta^{-1} \mathcal{P}, \quad \alpha = \frac{R \rho_s T_s}{p_s}, \quad (6)$$

where  $\mu_0$  is the vacuum permeability,  $R$  is the gas constant, and  $T_s$  is the constant temperature of the system. The parameter  $\Lambda$  and the product  $\mathcal{P}\alpha$  represent the nondimensional squared Alfvén speed and squared isothermal speed of sound respectively, scaled with the square of the freefall speed;  $\mathcal{U}_\Omega$  is the nondimensional rotation rate, and the plasma  $\beta$  denotes the ratio of the gas pressure to twice the magnetic pressure,  $\beta = \mu_0 p_s / B_s^2$ . Owing to the choice of a different scaling for the velocity in the  $x$ -direction, the dimensionless velocity in Equations (1)–(3) has the form  $\mathbf{u} = \mathcal{U}_u u \mathbf{e}_x + v \mathbf{e}_y + w \mathbf{e}_z$ , where

$$\mathcal{U}_u = \frac{U_s}{\sqrt{gd}} \quad (7)$$

is the ratio of a typical shear flow speed to the freefall speed. Positive (negative) values of  $\mathcal{U}_u$  correspond to eastward (westward) flows.

To determine the basic state, the linear stability of which we shall investigate, we consider a layer of fluid in equilibrium, in the region  $0 \leq z \leq 1$ , with a shear flow  $\mathbf{u}_0(z)$  and horizontal magnetic field  $\mathbf{B}_0(z)$ , as described above. The basic-state density  $\rho_0(z)$  and pressure  $p_0(z)$  are then determined by the equations

$$D(\mathcal{P}p_0(z) + \Lambda a_0^2(z)/2) = (\mathcal{U}_\Omega \mathcal{M}_u u_0(z) - f) \rho_0(z), \quad (8)$$

$$p_0(z) = \alpha \rho_0(z), \quad (9)$$

where  $D$  denotes  $d/dz$ , together with  $\rho_0(1) = 1$  (recall,  $\rho_s$  was chosen as the density value at the top of the fluid layer). In addition, in order to identify clearly the effect of buoyancy, we introduce the parameter  $f$ , which takes the value 1 if the buoyancy force is present in the momentum equation, and 0 if it is not.

At this stage, we also define the following functions of the basic-state variables:

$$F(z) = \Lambda a_0^2(z) + \mathcal{P}\alpha \rho_0(z), \quad H_U^{-1}(z) = u_0^{-1}(z) D u_0(z), \quad (10a,b)$$

$$H_\rho^{-1}(z) = \rho_0^{-1}(z) D \rho_0(z), \quad H_B^{-1}(z) = a_0^{-1}(z) D a_0(z), \quad (10c,d)$$

where  $F(z)$  is related to the speed of isothermal magnetosonic waves, and where  $H_U^{-1}(z)$ ,  $H_\rho^{-1}(z)$ , and  $H_B^{-1}(z)$  are the depth-dependent inverse scale heights of shear flow, density, and

magnetic field respectively. We also note that the basic-state equations (8)–(9) imply the following relation:

$$\mathcal{P}\alpha H_\rho^{-1}(z) = (-\Lambda a_0^2(z)/\rho_0(z)) H_B^{-1}(z) - (f - \mathcal{U}_\Omega \mathcal{M}_u u_0(z)). \quad (11)$$

In order to simplify what is quite a complicated problem, we assume, as did Mizerski et al. (2013), Gradzki & Mizerski (2018), that the perturbations to the basic state take the form of interchange (“axisymmetric”) modes, i.e., all perturbation quantities are invariant in the  $x$ -direction (parallel to the direction of the basic-state toroidal magnetic field and the basic shear flow). Owing to the homogeneity of the system in the  $y$ -direction, a simple Fourier-mode type dependence is assumed, with the wavenumber denoted by  $k$  and the growth rate by  $\sigma$ . We thus express perturbations to the velocity, magnetic field, pressure, and density as

$$\begin{aligned} \tilde{\mathbf{u}} &= (\tilde{u}(z), \tilde{v}(z), \tilde{w}(z)) e^{\sigma t + iky}, \quad \tilde{\mathbf{B}} = (\tilde{a}(z), \tilde{b}(z), \tilde{c}(z)) e^{\sigma t + iky}, \\ \tilde{p}(z) &e^{\sigma t + iky}, \quad \tilde{\rho}(z) e^{\sigma t + iky}. \end{aligned} \quad (12)$$

On introducing perturbations of the form (12) into Equations (1)–(5) and neglecting nonlinear terms, we obtain the following system of linear equations:

$$(\mathcal{U}_u \sigma \rho_0) \tilde{u} + (\mathcal{U}_u \rho_0 D u_0) \tilde{w} = (i\Lambda k b_0) \tilde{a} + (\Lambda D a_0) \tilde{c} - (\mathcal{U}_\Omega \rho_0) \tilde{w}, \quad (13a)$$

$$(\sigma \rho_0) \tilde{v} = -ik(\mathcal{P}\tilde{p} + \Lambda a_0 \tilde{a}), \quad (13b)$$

$$\begin{aligned} (\sigma \rho_0) \tilde{w} &= -D(\mathcal{P}\tilde{p} + \Lambda a_0 \tilde{a}) - (\Lambda b_0) D \tilde{b} + (i\Lambda k b_0) \tilde{c} \\ &+ (\mathcal{U}_\Omega \mathcal{M}_u u_0 - f) \tilde{p} + (\mathcal{U}_\Omega \mathcal{M}_u \rho_0) \tilde{u}, \end{aligned} \quad (13c)$$

$$\sigma \tilde{p} + (ik \rho_0) \tilde{v} + (D \rho_0) \tilde{w} + \rho_0 D \tilde{w} = 0, \quad (13d)$$

$$\sigma \tilde{a} + (D a_0) \tilde{w} = (i\mathcal{U}_u k b_0) \tilde{u} + (\mathcal{U}_u D u_0) \tilde{c} - (i k a_0) \tilde{v} - a_0 D \tilde{w}, \quad (13e)$$

$$\sigma \tilde{b} = -b_0 D \tilde{w}, \quad (13f)$$

$$\sigma \tilde{c} = (i k b_0) \tilde{w}, \quad (13g)$$

$$(i k) \tilde{b} + D \tilde{c} = 0, \quad (13h)$$

$$\tilde{p} = \alpha \tilde{\rho}. \quad (13i)$$

Equations (13a–i) can be manipulated to yield a single second-order ordinary differential equation for the  $z$ -dependent amplitude of the vertical velocity perturbation  $\tilde{w}(z)$ , with the growth rate  $\sigma$  determined as the eigenvalue of the problem. We may express this differential equation in the general form

$$\left[ \tilde{W}_2(z) \right] D^2 \tilde{w}(z) + \left[ \tilde{W}_1(z) \right] D \tilde{w}(z) + \left[ \tilde{W}_0(z) \right] \tilde{w}(z) = 0, \quad (14)$$

where the coefficients  $\tilde{W}_0(z)$ ,  $\tilde{W}_1(z)$ , and  $\tilde{W}_2(z)$  depend on the basic-state functions and their derivatives, the horizontal wavenumber  $k$ , the growth rate  $\sigma$ , and the various dimensionless constants of the system. The top and bottom boundaries are assumed impermeable, which implies the boundary conditions

$$\tilde{w} = 0 \quad \text{on } z = 0, 1. \quad (15)$$

Equation (14) with boundary conditions (15) constitutes a second-order boundary value problem, with the growth rate  $\sigma$

appearing as the eigenvalue. The coefficients of Equation (14) are, though, very complicated and hence, in general, Equation (14) requires a numerical solution. However, under certain assumptions, it is possible to make analytic progress through an asymptotic Rayleigh–Schrödinger perturbation approach. Such an approach is described by Griffiths (2008; for inertial instabilities), Mizerski et al. (2013; for nondiffusive MBI), and Gradzki & Mizerski (2018; for diffusive MBI).

In our analytical study, we assume that all the basic-state functions and their derivatives, the growth rate  $\sigma$ , and the dimensionless parameters are of order unity in terms of any asymptotic parameters in the theory. As argued first by Gilman (1970), the growth rate of the MBI, in the absence of diffusion, increases with increasing transverse wavenumber  $k$ , tending to some finite value as  $k \rightarrow +\infty$ . Thus, the limit of  $k \rightarrow +\infty$  is the first asymptotic limit assumed here. Furthermore, in some natural systems, such as, for example, the solar tachocline, the poloidal magnetic field is expected to be relatively weak in comparison with the toroidal component. It thus turns out to be instructive to assume a second asymptotic limit of  $b_0 \rightarrow 0$ .

In general, one must construct double asymptotic expansions in the two small parameters: the inverse wavenumber  $k^{-1}$  and the weak poloidal magnetic field  $b_0$ . However, since we are interested in investigating interactions between MBI, MRI, and CI, we assume that  $k \sim b_0^{-1}$ , which not only simplifies the asymptotic analysis to one small parameter but also ensures that the contributions to the growth rate of perturbations from all three instability types are of comparable order of magnitude. In other words, it is only for a weak field  $b_0$  that the three instability mechanisms are captured at leading order; this assumption is also consistent with the linear MRI analysis presented by Balbus & Hawley (1991). Further justification for this assumption is given in Appendix B. To summarize, we shall show that the assumptions

$$k \rightarrow +\infty, \quad b_0 \rightarrow 0, \quad k \sim b_0^{-1} \quad (16)$$

allow the presence of all possible types of instability at the leading order of the asymptotic approach, thus providing the opportunity to study their mutual interactions and competition. The relation  $k \sim b_0^{-1}$  establishes the horizontal spatial scale of the interchange perturbations given by (12) by relating it to the weak magnitude of the constant poloidal magnetic field  $b_0$ .

### 3. Leading Order Asymptotic Analysis

The full details of the leading order asymptotic analysis are presented in Appendix C; here we provide the most important results, together with an explanation of the method adopted. The first stage of the analysis leads to the conclusion that all possible eigenvalues  $\sigma$  of the system of equations (13a–i) have their leading (zeroth) order asymptotic approximations, namely  $\sigma_0$ , in the image of the  $z$ -dependent function called the *growth rate function*, denoted as  $\sigma(z)$ . This function is given implicitly by the leading order solution of the quartic equation  $\tilde{W}_0(z) = 0$ , where  $\tilde{W}_0(z)$  is the coefficient of  $\tilde{w}$  in Equation (14), defined by Equations (A1c) and (A2c). Hence, the leading order values  $\sigma_0$  of all the growth rates are determined by the growth rate function  $\sigma(z)$  evaluated at initially unknown points  $z_0$ , called the *evaluation points*. That is, for one particular eigenmode, we have  $\sigma_0 = \sigma(z_0)$ , for some  $z_0 \in [0, 1]$ . With every eigenvalue  $\sigma$ , there is an associated eigenmode  $\tilde{w}(z)$ , which is a solution of

Equation (14). Based on the form of Equation (14), we can anticipate boundary layer-type, highly localized solutions (see Mizerski et al. 2013; Gradzki & Mizerski 2018). However, the precise spatial structure of the eigenmodes can be determined only by considering first-order corrections to the growth rate  $\sigma$ ; hence, solving for the mode structure is postponed until Section 4.

Determining the set of allowed evaluation points  $z_0$  is tantamount to finding the leading order spectrum of the linear differential operator given by the system of Equations (13a–i). Our Rayleigh–Schrödinger perturbation analysis shows that there are two distinct types of eigenmode. First, the eigenmodes may be associated with the evaluation points  $z_0$  lying on the boundaries of the domain, that is  $z_0 = 0$ , or  $z_0 = 1$ ; we refer to these boundary layer-type solutions as *wall modes*. Second, eigenmodes with an internal layer type may exist for evaluation points  $z_0$  lying strictly in the domain  $0 < z_0 < 1$ ; we refer to these solutions as *body modes*. However, the detailed characteristics of all these eigenmodes, as well as the determination of the evaluation points of the body modes, are obtained by consideration of the next-order corrections to the growth rate  $\sigma$  (see Section 4 and Appendix D).

In addition to eigenmodes with a highly localized structure, there may also exist WKB modes, with oscillations throughout the bulk of the layer, on intervals determined by the evaluation points  $z_0$  and the form of the growth rate function  $\sigma(z)$ . However, as shown by Mizerski et al. (2013) for the pure MBI, the WKB solutions are always less unstable, characterized by lower values of  $\Re(\sigma_0)$  than the boundary layer modes. Numerical simulations confirm that this remains the case for the more complicated setup considered here. Therefore, in any temporal linear evolution, the most unstable boundary layer mode (be it a wall mode or a body mode) will ultimately dominate.

From the governing ordinary differential equation (14), the leading order contribution to the growth rate  $\sigma_0$  associated with the evaluation point  $z_0$  is a solution of the quartic equation (see Equation (C6))

$$A_4(z_0)\sigma_0^4 + A_2(z_0)\sigma_0^2 + A_1(z_0)\sigma_0 + A_0(z_0) = 0, \quad (17)$$

where the coefficients  $A_n$ , given by (A3a–d), are functions of the basic-state variables, the set of parameters (6), and positive integer powers of the product  $kb_0$ . In particular, under the assumptions (16),  $\sigma_0$  does not depend separately on  $k$  or  $b_0$ . The value of  $b_0$  establishes the order of magnitude for the wavenumber  $k$  of the eigenmodes; a similar idea arose in the treatment of magnetic diffusivity by Gradzki & Mizerski (2018).

In general, for a given value of  $z_0$ , the four solutions  $\sigma_0$  of Equation (17) are complex. If there exists at least one solution with  $\Re(\sigma_0) > 0$ , the associated eigenmode  $\tilde{w}(z)$  is unstable. In general, any instability involves coupling between the three types of instabilities: MRI, MBI, and CI. Although there are closed algebraic formulae for the solutions of any quartic equation, they are somewhat unwieldy. Therefore, it is not possible to give a general simple formula for  $\sigma_0$  and hence a general stability criterion. However, for a fixed value of the evaluation point  $z_0$ , the algebraic Equation (17) can be solved numerically in a straightforward manner for any specific values of the system parameters (6). Furthermore, for some important cases, Equation (17) reduces to a biquadratic, with relatively simple analytic solutions. This happens for any “subcase” of the full system, defined by neglect of one or more of the

following factors: rotation  $\Omega$ , shear flow  $u_0(z)$ , toroidal field  $a_0(z)$ , or poloidal field  $b_0$ . For each of these subcases, we need consider only an individual instability mechanism or a coupling of at most two. An analysis of the various subcases allows us to investigate the constituent parts of the instability of the complete system, and to make comparison with earlier studies. In the following subsections, we present the analytical approach to these subcases, which prepares the ground for the detailed analysis of the full system.

### 3.1. Centrifugal Instability

If we neglect the effect of the magnetic field, namely we set  $a_0(z) = 0$ , and  $b_0 = 0$  in the system of Equations (13a–i), and hence also in Equation (17), we obtain a purely hydrodynamic system, with the only possibility of instability being centrifugal. In this case, the growth rate at leading order,  $\sigma_0$ , which we denote by  $\sigma_{\text{CI}}$ , is given by the simple expression

$$\sigma_{\text{CI}}^2(z_0) = -\kappa^2(z_0), \quad (18)$$

where

$$\kappa^2(z) = \mathcal{U}_\Omega(\mathcal{U}_\Omega - \mathcal{U}_u(-Du_0(z))) \quad (19)$$

is the square of the depth-dependent nondimensional local form of the epicyclic frequency  $\kappa$ , which is the frequency of oscillations of a radially displaced fluid parcel in a differentially rotating system (see Balbus & Hawley 1991).

It can be seen that in the absence of a basic-state shear flow  $u_0(z)$ ,  $\kappa^2 > 0$ , and so the system supports only waves with rotational frequency  $\mathcal{U}_\Omega > 0$ . However, in the presence of a shear flow, instability will ensue if  $\kappa^2(z_0) < 0$  at some level  $z_0$  in the fluid layer; equivalently

$$\mathcal{U}_u(-Du_0(z_0)) > \mathcal{U}_\Omega \text{ for some } z_0. \quad (20)$$

Inequality (20) is a local equivalent of the well-known Rayleigh criterion for a differentially rotating fluid; namely that, for a given radial profile of the angular velocity  $\Omega(R)$ , a necessary condition for instability is that the fluid specific angular momentum  $R^2\Omega(R)$  must decrease with increasing distance  $R$  from the rotation axis, i.e.,  $d(R^2\Omega(R))/dR < 0$ . This inequality may be rewritten as  $2\Omega(2\Omega + Rd\Omega/dR) < 0$ , where the left-hand side of this inequality is the standard definition of the epicyclic frequency for a differentially rotating fluid. It agrees with our local model, in which the rotation parameter  $\mathcal{U}_\Omega$  and the shear flow gradient  $\mathcal{U}_u Du_0$  correspond to the quantities  $2\Omega(R)$  and  $Rd\Omega(R)/dR$  respectively. For the particular case when the basic flow  $u_0(z)$  is a linear function of  $z$  with negative gradient (i.e., the epicyclic frequency  $\kappa$  is constant), our model reduces to a standard shearing box approximation. However, our asymptotic analysis is valid for an arbitrary shear flow profile  $u_0(z)$ . It follows that, for the full system governed by Equations (13a–i), we can expect that a threshold value of the flow gradient, at which the squared epicyclic frequency  $\kappa^2(z)$  first becomes negative somewhere in the layer, will play an important role in the dynamics.

### 3.2. Magnetorotational Instability

For the less restrictive system in which the poloidal component is retained, but the basic-state toroidal magnetic field is still neglected (i.e., we set  $a_0(z) = 0$ , and  $b_0 \neq 0$  in

Equations (13a–i)), besides the CI, we may also expect the occurrence of the axisymmetric MRI. In general, the MRI occurs when, in a rotating magnetized fluid, the angular velocity decreases with radius. However, we demonstrate in Appendix C that, under the assumption of weak poloidal field ( $b_0 \rightarrow 0$ ), the MRI instability is apparent at leading order only for high wavenumbers satisfying  $k \sim b_0^{-1}$ . The other regimes, namely  $1 \ll k \ll b_0^{-1}$  and  $k \gg b_0^{-1} \gg 1$ , lead to the pure CI (if  $\kappa^2(z_0) < 0$ ) and stability (at least at leading order), respectively. This is a well-known result for weak magnetic fields (e.g., Balbus & Hawley 1991).

By the use of Equation (17), for the case at hand, the leading order contribution to the growth rate  $\sigma_0 \equiv \sigma_{\text{MRI}}$  takes the following form (see Expression (B5)):

$$\sigma_{\text{MRI}}^2(z_0) = -\frac{k^2 b_0^2}{\rho_0(z_0)/\Lambda} - \frac{\kappa^2(z_0)}{2} + \left[ \mathcal{U}_\Omega^2 \frac{k^2 b_0^2}{\rho_0(z_0)/\Lambda} + \left( \frac{\kappa^2(z_0)}{2} \right)^2 \right]^{1/2}. \quad (21)$$

An important difference from the pure CI case, with growth rate given by Equation (18), is that now, at leading order, the growth rate depends on the wavenumber  $k$ . Thus, the corresponding growth rate function is dependent on both height and wavenumber,  $\sigma(z, k)$ , which makes the identification of the most unstable mode somewhat more complicated. It is instructive to consider separately the cases of  $\kappa^2(z_0) < 0$ , for which case the CI is present in the absence of magnetic field, and  $\kappa^2(z_0) > 0$ , for which it is not.

If  $\kappa^2(z_0) < 0$ , there is instability provided that

$$0 < \frac{k^2 b_0^2}{\rho_0(z_0)/\Lambda} < \mathcal{U}_\Omega^2 - \kappa^2(z_0), \quad (22)$$

thus showing that the CI is eventually stabilized by a sufficiently large value of  $kb_0$ . If

$$\mathcal{U}_\Omega^2 + \kappa^2(z_0) > 0, \quad (23)$$

then the CI is initially destabilized by the inclusion of a very weak magnetic field, before eventually being stabilized as the field strength (or, to be more precise, the product  $kb_0$ ) is increased. If, on the other hand, Inequality (23) is not satisfied, then increasing the magnetic field strength  $b_0$  is monotonically stabilizing.

It is when  $\kappa^2(z_0) > 0$ , and hence when the flow is stable to CI in the absence of  $b_0$ , that the influence of the magnetic field becomes particularly significant. In this case, from Expressions (19) and (21), the criterion for instability—to an axisymmetric MRI—takes the following form:

$$\mathcal{U}_\Omega^2 - \kappa^2(z_0) = \mathcal{U}_\Omega \mathcal{U}_u(-Du_0(z_0)) > \frac{k^2 b_0^2}{\rho_0(z_0)/\Lambda}, \quad (24)$$

which is a local form of the standard criterion for the MRI,  $-Rd\Omega^2(R)/dR > k^2 b_0^2 / (\mu\rho_0)$  (see Balbus & Hawley 1991). Hence, in our system, the rotation rate or the negative shear flow gradient must be sufficiently strong in order to destabilize the flow. On the other hand, without rotation ( $\mathcal{U}_\Omega = \kappa = 0$ ), Expression (21) simply reduces to the dispersion relation for Alfvén waves, whereas with rotation but no shear

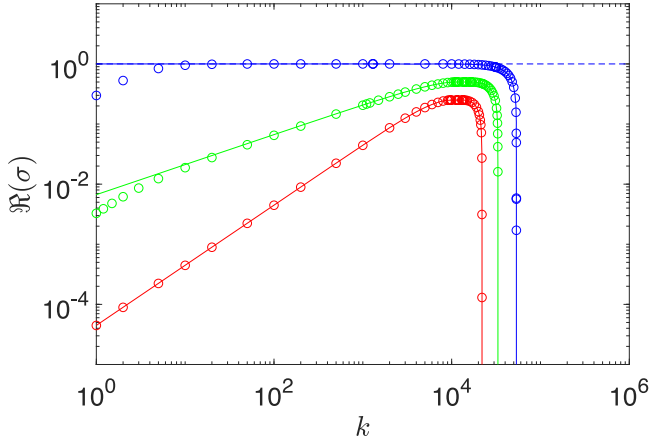


**Figure 2.** Positive branches of the real parts of the growth rates  $\Re(\sigma(k))$  as functions of wavenumber  $k$  for a system that is unstable owing to the MRI or CI. The basic state has a linear shear flow of the form  $u_0(z) = -\zeta z$ , with  $\zeta = 0.5$  (red),  $\zeta = 1.0$  (green), and  $\zeta = 2.0$  (blue). The values of the remaining parameters are  $a_0 = 0$ ,  $b_0 = 10^{-4}$ ,  $\Lambda = 0.2$ ,  $\mathcal{U}_u = 1.0$ ,  $\mathcal{U}_\Omega = 1.0$ ,  $\mathcal{P} = 1.9$ ,  $\alpha = 1.0$ ,  $f = 1$ . Solid lines denote the leading order growth rate  $\sigma_0$ ; circles denote the numerically determined eigenvalues  $\sigma$ . The blue dashed line indicates the wavenumber-independent analytical value of  $\sigma_0$  for the pure CI subcase (with  $b_0 = 0$ ).

( $Du_0 = 0 \Leftrightarrow \mathcal{U}_\Omega^2 = \kappa^2 > 0$ ), such waves are coupled with inertial waves. In both cases, the system is always stable, i.e.,  $\sigma_{\text{MRI}}^2 \leq 0$ .

From Expression (21), it is straightforward to show that the wavenumber of the mode of maximum growth rate, for fixed  $b_0$ , is given by

$$k = k_{\text{MRI}} = b_0^{-1} \left[ \frac{\rho_0(z_0) (\mathcal{U}_\Omega^4 - \kappa^4(z_0))}{\Lambda 4\mathcal{U}_\Omega^2} \right]^{1/2}, \quad (25)$$

with associated maximum growth rate given by

$$\sigma^2 = \sigma_{\text{MRI}}^2(z_0, k_{\text{MRI}}) = \frac{(\mathcal{U}_\Omega^2 - \kappa^2(z_0))^2}{4\mathcal{U}_\Omega^2}. \quad (26)$$

As noted by Balbus & Hawley (1991), although the wavenumber of the mode of maximum growth rate, given by Expression (25), depends on  $b_0$ , the maximum growth rate itself, given by Equation (26), does not. It is also worth noting that Expressions (25) and (26) are in accord with those for an isothermal, incompressible Keplerian disk, for which the preferred mode is given by  $k_{\text{MRI}}^2 b_0^2 = 15\rho_0 \mathcal{U}_\Omega^2 / 64\Lambda$ , with maximum growth rate given by  $\sigma_{\text{MRI}} = 3\mathcal{U}_\Omega / 8$ .

Expression (25) in fact defines a range of wavenumbers for all possible evaluation points  $z_0 \in [0, 1]$ , with corresponding growth rates  $\sigma_{\text{MRI}}$  given by (26). In particular, for the simplest form of the basic shear flow  $u_0(z)$ , namely a linear shear (where the epicyclic frequency  $\kappa$  is constant), all modes with wavenumbers  $k \in k_{\text{MRI}}(z_0)$  have the same growth rate at leading order, namely  $\sigma_{\text{MRI}}(k_{\text{MRI}})$ ; the difference appears only in the higher-order analysis, which is described in Section 4 for the general case. Thus, for a linear shear, we expect a plateau in the dispersion relation  $\sigma(k)$  in the range between the minimum and maximum values of  $k_{\text{MRI}}$ . For a basic-state shear flow with a nonlinear dependence on  $z$ , the dispersion relation is more complicated, and depends on the form of the depth-dependent epicyclic frequency  $\kappa(z)$ .

As a specific example to illustrate the relationship between the asymptotic results (valid for  $k \gg 1$ ) and the numerical results (which can be obtained for all  $k$ ), we consider basic states with a uniform linear shear flow; thus we set  $u_0(z) = -\zeta z$ , with  $\zeta > 0$  to allow for the possibility of CI and MRI. Figure 2 shows selected positive branches of the real parts of  $\sigma(k)$  for three cases, differing only in the value of  $\zeta$ , chosen to highlight the role of the CI and MRI: the state with  $\zeta = 2$  is unstable to CI; that with  $\zeta = 0.5$  is stable to CI; and that of  $\zeta = 1$  is marginally stable. The theoretical relationship (21) is shown as solid lines, where the highest growth rate value  $\sigma_0$  is determined over the range of wavenumber values  $k$ ; there is clearly a preferred wavenumber that maximizes the growth rate. For comparison, the blue dashed line denotes the wavenumber-independent growth rate for the nonmagnetic case ( $b_0 = 0$ ) with  $\zeta = 2$ , where we can, at most, expect only CI, as described in Section 3.1. The numerically determined eigenvalues  $\sigma$  (marked by circles on Figure 2) are obtained from the full Equation (14) (with basic toroidal field  $a_0(z)$  set to zero); the numerical method of solution is described in detail in Section 5. From Figure 2, we can see, as noted above, that a weak constant poloidal magnetic field  $b_0$  can destabilize the system with respect to the pure CI ( $\zeta = 0.5$ , and  $\zeta = 1.0$  cases). However, if the shear gradient  $\zeta$  is increased, with all other parameters fixed (which also implies enhancement of the magnitude of the negative squared epicyclic frequency  $\kappa^2$ ), the CI eventually become so vigorous that there is no noticeable impact of the magnetic field on the growth rate  $\sigma$ . Nevertheless, the field  $b_0$  establishes a range of wavenumbers  $k$  for instability, given by Inequality (24), which is accurately captured by the numerically determined solutions. Of particular note in Figure 2 is the excellent agreement at large  $k$  between the analytical expression for the growth rate  $\sigma_{\text{MRI}}$ , given by Equation (21), and the value of  $\sigma$  determined numerically from Equation (14). Indeed, although our asymptotic results are obtained under the assumption  $k \sim b_0^{-1} \gg 1$ , the agreement between analytical and numerical results is very good even for  $k = O(10)$ . Moreover, this agreement can be improved by taking into account the next-order corrections to  $\sigma$ , as described in Section 4.

### 3.3. MBI of a Toroidal Field, with Shear Flow and Rotation

The pure axisymmetric MBI, in the absence of poloidal field, shear flow, and rotation, was studied in the limit of  $k \rightarrow \infty$  by Mizerski et al. (2013). Here, through similar methods, we investigate the influence of shear flow and rotation on the MBI of a toroidal field. From Equation (17), we can express the leading order growth rate  $\sigma_0$ , which we shall denote by  $\sigma_{\text{MBI}\kappa}$ , as

$$\sigma_{\text{MBI}\kappa}^2(z_0) = \sigma_{\text{MBI}}^2 + \sigma_{\text{MBIC}}^2 - \kappa^2(z_0). \quad (27)$$

In Equation (27),  $\sigma_{\text{MBI}}^2$  is the growth rate at leading order of the pure MBI (when  $\mathcal{U}_\Omega = \kappa = 0$ ) at a given evaluation point  $z_0$  (see Equation (35) in Mizerski et al. 2013), given by

$$\sigma_{\text{MBI}}^2(z_0) = \frac{\Lambda a_0^2(z_0) f}{F(z_0)} \left[ H_\rho^{-1}(z_0) - H_B^{-1}(z_0) \right]. \quad (28)$$

The expression for  $\sigma_{\text{MBIC}}^2$  is analogous, but with gravity replaced by the  $z$ -component of the Coriolis force:

$$\sigma_{\text{MBIC}}^2(z_0) = -\frac{\Lambda a_0^2(z_0) \mathcal{U}_\Omega \mathcal{U}_u u_0(z_0)}{F(z_0)} \left[ H_\rho^{-1}(z_0) - H_B^{-1}(z_0) \right]. \quad (29)$$

It can be seen from (28) that the pure MBI of an axisymmetric (interchange) mode is driven by a decrease in height of  $B/\rho$ , a result that may be recovered from a standard fluid parcel argument (e.g., Acheson 1979). The influence of uniform rotation is represented by a negative final term in (27), and hence is such that it always suppresses the instability, in accordance with previous studies (e.g., Gilman 1970; Acheson 1979). The influence of the shear flow  $u_0(z_0)$ , on the other hand, is more subtle, since it can either stabilize or destabilize the system. First, the horizontal basic flow affects the effective gravity through the Coriolis force (the Eötvös effect). Second, the sign of the shear flow gradient (or the epicyclic frequency squared,  $\kappa^2$ ) determines whether or not the shear will amplify the MBI.

The growth rate in the form (27) may be regarded as a coupling of the growth rates of the effective MBI (the first two terms) and the CI. We observe that the CI can be amplified by a sufficiently strong negative gradient of the toroidal magnetic field. We note that in this case the Coriolis force acts as an effective gravity (contributing to  $g$ ). Through this effect, the MBI is enhanced provided that the shear flow  $u_0(z)$  is negative (westward).

### 3.4. MBI with Poloidal Magnetic Field

As a final subcase, we consider the separate influence of the constant weak poloidal field  $b_0$  on the MBI, in the absence of both rotation ( $\mathcal{U}_\Omega = 0$ ) and shear flow ( $u_0 = 0$ ). As for the MRI subcase described in Section 3.2 and Appendix B, it can be shown that under the assumptions of short perturbation wavelengths (essential for the MBI) and weak field  $b_0$ , there are three possible regimes. The regime  $1 \ll k \ll b_0^{-1}$  yields the pure MBI, as in Mizerski et al. (2013), while for  $k \gg b_0^{-1} \gg 1$  there is no instability at leading order. There is a leading order influence of the poloidal magnetic field  $b_0$  on the growth rate only for  $k \sim b_0^{-1}$ . For this range of wavenumbers, Equation (17) reduces to a quadratic in  $\sigma_0^2$ , with the greater root taking the form

$$\sigma^2 = \sigma_{\text{MBIP}}^2(z_0) = \frac{1}{2} \left( \sigma_{\text{MBI}}^2 - \phi(z_0) \right) + \frac{1}{2} \left[ \left( \sigma_{\text{MBI}}^2 - \phi(z_0) \right)^2 + 4\psi(z_0) \right]^{1/2}, \quad (30)$$

where the functions  $\phi(z)$  and  $\psi(z)$  are defined as

$$\phi(z) = \frac{k^2 b_0^2 \Lambda}{\rho_0(z)} \left( 1 + \frac{\mathcal{P}\alpha \rho_0(z)}{F(z)} \right), \quad (31)$$

$$\psi(z) = \frac{k^2 b_0^2 \Lambda}{\rho_0(z)} \left( \frac{\mathcal{P}\alpha \rho_0(z)}{F(z)} \right) \left[ \sigma_{\text{MBI}}^2 - \left( \frac{k^2 b_0^2 \Lambda}{\rho_0(z)} - \frac{f^2 \Lambda a_0^2(z)}{\mathcal{P}\alpha F(z)} \right) \right]. \quad (32)$$

On using the basic-state Equation (11), with  $\mathcal{U}_\Omega = 0$ , the growth rate of the pure MBI ( $\sigma_{\text{MBI}}$ ), defined by (28), may be

expressed in terms of the inverse scale height of the toroidal magnetic field  $H_B^{-1}(z)$  as

$$\sigma_{\text{MBI}}^2(z_0) = \frac{f \Lambda a_0^2(z_0)}{\mathcal{P}\alpha \rho_0(z_0)} \left[ -H_B^{-1}(z_0) - \frac{f \rho_0(z_0)}{F(z_0)} \right]. \quad (33)$$

Moreover, it can be seen from Expression (30) that the growth rate (at leading order) of the MBI becomes dependent on the wavenumber  $k$  in the presence of a constant weak poloidal magnetic field  $b_0$ , or, in other words, that the growth rate function is now depth and wavenumber dependent, i.e.,  $\sigma = \sigma(z, k)$ . It can also be shown that  $\sigma_{\text{MBIP}}^2$  is always real; hence, the growth rate  $\sigma_{\text{MBIP}}$  can take either real or purely imaginary values, just like  $\sigma_{\text{MBI}}$ .

Expression (30) yields a simple instability criterion, which may be expressed as a condition on the inverse magnetic field scale height at a point  $z_0$  somewhere in the fluid layer:

$$-H_B^{-1}(z_0) > \frac{k^2 b_0^2 \mathcal{P}\alpha}{f a_0^2(z_0)} > 0. \quad (34)$$

With the aid of Equation (33), Criterion (34) can be rearranged into the following form:

$$\frac{k^2 b_0^2 \Lambda}{\rho_0(z_0)} < \sigma_{\text{MBI}}^2 + \frac{f^2 \Lambda a_0^2(z_0)}{\mathcal{P}\alpha F(z_0)}, \quad (35)$$

or, equivalently,

$$1 \ll k \lesssim b_0^{-1} \left[ \frac{\rho_0(z_0)}{\Lambda} \left( \frac{f^2 \Lambda a_0^2(z_0)}{\mathcal{P}\alpha F(z_0)} + \sigma_{\text{MBI}}^2 \right) \right]^{1/2}. \quad (36)$$

Thus, any system that is unstable at a point  $z_0$  with respect to the pure MBI ( $\sigma_{\text{MBI}} > 0$ ) will always be unstable ( $\sigma_{\text{MBIP}} > 0$ ) in the presence of a weak field  $b_0$  for some range of large wavenumbers  $k$ , provided that the asymptotic assumption  $1 \ll k \sim b_0^{-1}$  is also satisfied. An interesting consequence of Criterion (36) is that it can be satisfied even for  $\sigma_{\text{MBI}}^2 < 0$ , provided that the condition  $H_B^{-1}(z_0) < 0$  is met. Thus, a poloidal field  $b_0$  can destabilize an eigenmode associated with the evaluation point  $z_0$  that is stable as a result of pure MBI.

Just as in the subcase of the pure MRI presented in Section 3.2 (see also Appendix B), we can find the range of wavenumbers  $k$  for the most unstable modes, since Expression (30) for the growth rate  $\sigma_{\text{MBIP}}$  depends explicitly on  $k$ . It is readily shown that the critical wavenumber  $k = k_{\text{MBIP}}$  is determined by a biquadratic equation. Since, without loss of generality, we may concentrate on positive values of  $k_{\text{MBIP}}$ , it can be demonstrated that there can be at most one positive solution  $k_{\text{MBIP}} > 0$ , which exists if the following condition is satisfied:

$$-\left( \frac{f^2 \rho_0}{F} \right) \left( \frac{\Lambda a_0^2}{\mathcal{P}\alpha \rho_0} \right) < \sigma_{\text{MBI}}^2 < \left( \frac{f^2 \rho_0}{F} \right) \left( \frac{\Lambda a_0^2}{F} \right); \quad (37)$$

for succinctness, we have omitted the argument  $z_0$  in all  $z$ -dependent functions, as we will also do in the subsequent expressions in this section. The interpretation of (37) is that, if the negative gradient of the toroidal magnetic field is too strong or too weak (making  $\sigma_{\text{MBI}}^2$  too large or “too negative”), the growth rate  $\sigma_{\text{MBIP}}$ , if positive, reaches its maximum value somewhere on the boundaries of the region defined by  $k \sim b_0^{-1}$

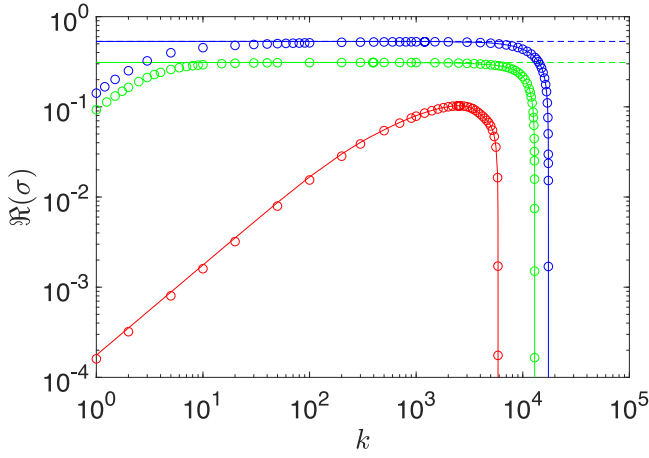


**Figure 3.** Positive branches of the real parts of the growth rates  $\Re(\sigma(k))$  as functions of the wavenumber  $k$ , for a system that is unstable to MBI in the presence of a weak constant poloidal field  $b_0$ , and in the absence of both rotation and a basic shear flow ( $\mathcal{U}_\Omega = u_0(z) = 0$ ). The basic-state toroidal magnetic field takes the form  $a_0(z) = 1 + \lambda(1 - z)$ , for  $\lambda = 0.45$  (red),  $\lambda = 1.35$  (green), and  $\lambda = 1.95$  (blue). The values of the remaining parameters are  $b_0 = 10^{-4}$ ,  $\Lambda = 0.2$ ,  $\mathcal{U}_u = 1.0$ ,  $\mathcal{P} = 1.9$ ,  $\alpha = 1.0$ ,  $f = 1$ . Solid lines denote the leading order growth rate  $\sigma_0$ ; circles denote the numerically determined eigenvalues  $\sigma$ . The dashed lines indicate the wavenumber-independent analytical value of  $\sigma_0$  for the pure MBI subcase with  $b_0 = 0$ .

and not in the form of a critical point  $k_{\text{MBIP}}$ . However, if Condition (37) is met, the growth rate  $\sigma_{\text{MBIP}}^2$  attains its (always positive) maximum given by the expression

$$\sigma_{\text{MBIP}}^2(k_{\text{MBIP}}, z_0) = \frac{\mathcal{P}\alpha\rho_0}{\Lambda a_0^2} \left( \sqrt{\frac{f^2\rho_0}{F} - \sigma_{\text{MBI}}^2} - \sqrt{\frac{f^2\rho_0}{\mathcal{P}\alpha\rho_0}} \right)^2, \quad (38)$$

with the wavenumber given by

$$k_{\text{MBIP}} = b_0^{-1} \left[ \frac{(F + \mathcal{P}\alpha\rho_0)f\rho_0}{\Lambda^2 a_0^2 (\mathcal{P}\alpha)^{1/2}} \left( \frac{f^2\rho_0}{F} - \sigma_{\text{MBI}}^2 \right)^{1/2} - \frac{F\rho_0}{\Lambda^2 a_0^2} \left( 2\frac{f^2\rho_0}{F} - \sigma_{\text{MBI}}^2 \right) \right]^{1/2}. \quad (39)$$

Expression (39) determines the range of wavenumbers of the most unstable modes  $k \in k_{\text{MBIP}}(z_0)$  for all evaluation points  $z_0 \in [0, 1]$  at the leading order of the asymptotic analysis.

We may also investigate the condition for enhancement of the MBI by inclusion of the field  $b_0$ , for the most unstable modes with growth rate  $\sigma_{\text{MBIP}}$  given by (38) and wavenumber  $k_{\text{MBIP}}$  given by (39), both calculated at the evaluation point  $z_0$  that maximizes  $\sigma_{\text{MBIP}}$ . The sufficient condition for  $\sigma_{\text{MBIP}}(k_{\text{MBIP}}) > \sigma_{\text{MBI}}$  takes the following simple form:

$$\sigma_{\text{MBI}}^2 < \left( \frac{f^2\rho_0}{F} \right) \left( 1 - \sqrt{\frac{\mathcal{P}\alpha\rho_0}{F}} \right)^2. \quad (40)$$

Therefore, if the pure MBI is not “too unstable”, the inclusion of the poloidal field  $b_0$  can enhance the growth rate, provided that Criterion (37) is also met.

Figure 3 shows selected positive branches of the real parts of the “dispersion relations”  $\sigma(k)$  for three sets of values of the system parameters. The theoretical relationship (solid lines) follows from Expression (30), where the highest value of the

growth rate at leading order,  $\sigma_0$ , is determined for each wavenumber  $k$ . This allows for identification of the range of wavenumbers of the most unstable modes. The dashed lines in Figure 3 mark the wavenumber-independent  $\sigma_0$  for the case of pure MBI with  $b_0 = 0$ , given by Expression (28). The numerical eigenvalues  $\sigma$  (marked by circles) are obtained from the full Equation (14) in the absence of both rotation and a basic shear flow ( $\mathcal{U}_\Omega = u_0(z) = 0$ ), and for a linear basic toroidal magnetic field of the form  $a_0(z) = 1 + \lambda(1 - z)$ , solved by the method described in Section 5.

From Figure 3, we can see that, in accordance with our theory, a weak constant poloidal magnetic field  $b_0$  establishes a finite wavenumber range of the most unstable modes with  $k \sim b_0^{-1}$ , suppressing the shorter perturbations to a zero growth rate. For a sufficiently strong gradient of the toroidal magnetic field (represented by the  $\lambda = 1.35$ , and  $\lambda = 1.95$  cases), with all other parameters fixed, the highest  $\sigma$  value achieved is very well approximated by the analytical growth rate at leading order,  $\sigma_0$ , from both (30) and (38). This growth rate is also almost equal to the eigenvalue  $\sigma$  of the most unstable modes for the case of pure MBI with  $b_0 = 0$ , when the finite wavenumber  $k$  of the most unstable modes cannot be established (the pure MBI growth rate is maximized when  $k \rightarrow \infty$ ). On the other hand, when the toroidal field gradient  $\lambda$  is relatively weak (as shown by the case of  $\lambda = 0.45$ ), so that the pure MBI is not excited, under Condition (40), the presence of the poloidal field  $b_0$  can destabilize the system; the growth rate of the most unstable mode is then very well approximated by (30) and (38). This is a somewhat surprising effect, since in our setup the poloidal field  $b_0$ , in the absence of a toroidal field  $a_0(z)$ , is not a source of any type of instability in a nonrotating system. It is the joint action of  $b_0$  and the weak toroidal field gradient that leads to destabilization.

### 3.5. Viewing the Full System through the Subcases

It is of interest to consider the role of the various subcases for different basic states, to determine which subcase, if any, dominates, together with the relationship between the full system and the various subcases. In this section, to address these points, we consider, as an illustrative example, two families of basic states, and within each, we explore the dependence on the basic-state shear flow  $u_0(z)$ . We consider the two sets of parameter values:

$$\begin{aligned} \mathcal{P} = 1.9, \quad \alpha = 1.0, \quad \Lambda = 0.2, \\ \lambda = 1.35, \quad \mathcal{U}_u = 1.0, \quad \mathcal{U}_\Omega = 1.0, \end{aligned} \quad (41)$$

and

$$\begin{aligned} \mathcal{P} = 1.9, \quad \alpha = 1.0, \quad \Lambda = 0.2, \\ \lambda = 1.95, \quad \mathcal{U}_u = 1.0, \quad \mathcal{U}_\Omega = 0.4, \end{aligned} \quad (42)$$

where the parameter  $\lambda$  is the constant gradient of the basic-state toroidal magnetic field,  $a_0(z) = 1 + \lambda(1 - z)$ . The basic-state shear flow is also taken to be linear with a negative gradient, which is necessary in order to excite the MRI and CI instabilities; thus  $u_0(z) = -\zeta z$ . The parameters (41) describe what we shall term as the *weak-MBI* case, since, for these parameter values, in the absence of the shear flow  $u_0(z)$ , the MBI is entirely suppressed by rotation, regardless of the presence of the poloidal field  $b_0$ . We shall refer to the case described by parameters (42), in which the MBI is not

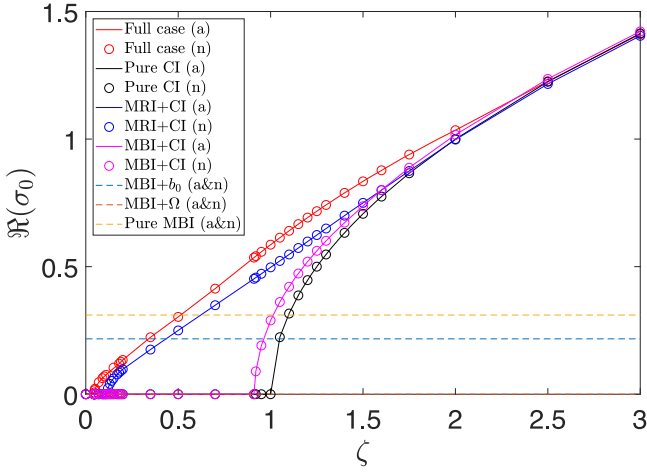


**Figure 4.** Positive branches of the real parts of the leading order growth rates of the most unstable modes of the full system and the various subcases, as a function of the basic shear flow gradient  $\zeta$  for the weak-MBI case, defined by (41). The poloidal magnetic field has magnitude  $b_0 = 1/k$ . Analytic results (a) are represented by solid lines, numerical results (n) by circles. Dashed lines denote the shear-independent cases explained in the legend.

suppressed by rotation in the absence of a shear flow  $u_0(z)$ , as the *strong-MBI* case.

Figure 4 (for the weak-MBI case) and Figure 5 (for the strong-MBI case) present theoretical (high wavenumber) values of  $\sigma_0$  (the leading order growth rate) and numerical values of  $\sigma$  (the full growth rate) for the most unstable modes, as a function of the basic shear flow gradient  $\zeta$ . The results for the various subcases are shown, together with those for the full system. Numerical results are obtained from solving the full Equation (14) for a wide range of wavenumbers  $k$ ; details of how the numerical results are obtained are contained in Section 5. In this subsection, for the numerical results, we follow our theoretical assumption and take  $b_0 = 1/k$ . It is, though, worth noting that from the results of Section 5, in which we fix the value of  $b_0$ , our assumption here on  $b_0$  is not particularly restrictive. It can be seen that there is excellent agreement between the analytical and numerical results.

Considering first the weak-MBI case, for sufficiently large shear gradients ( $\zeta \gtrsim 3$ ), the dynamics is dominated by the CI. However, for weaker shear, it can be seen that different instability types require different minimum values of  $\zeta$  to enter the dynamics. The pure CI is destabilized for  $\zeta > 1.0$ . However, with rotation present, a slightly lower value ( $\zeta \approx 0.91$ ) initiates the MBI, owing to the influence of the Coriolis force on the effective gravity. A significantly weaker threshold value ( $\zeta > 0.11$ ) is needed for emergence of the MRI, which turns out to be the most unstable subcase among the instabilities considered individually. Finally, the full system—including rotation, shear flow, and magnetic field (both poloidal and toroidal)—is destabilized by the weakest shear threshold ( $\zeta > 0.044$ ). From Figure 4, it can be seen that, for a given value of the shear gradient  $\zeta$ , the growth rate for the full case exceeds that of any of the subcases. This may be interpreted as the full system experiencing reinforcement from the component instability mechanisms. By contrast, Figure 4 also shows three shear-independent cases: the pure MBI, the MBI under the sole influence of the poloidal field  $b_0$ , and the MBI under the sole influence of rotation  $\Omega$ . It can be seen that the MBI in the absence of shear flow is entirely suppressed by rotation and significantly weakened by the poloidal field. With an increasing

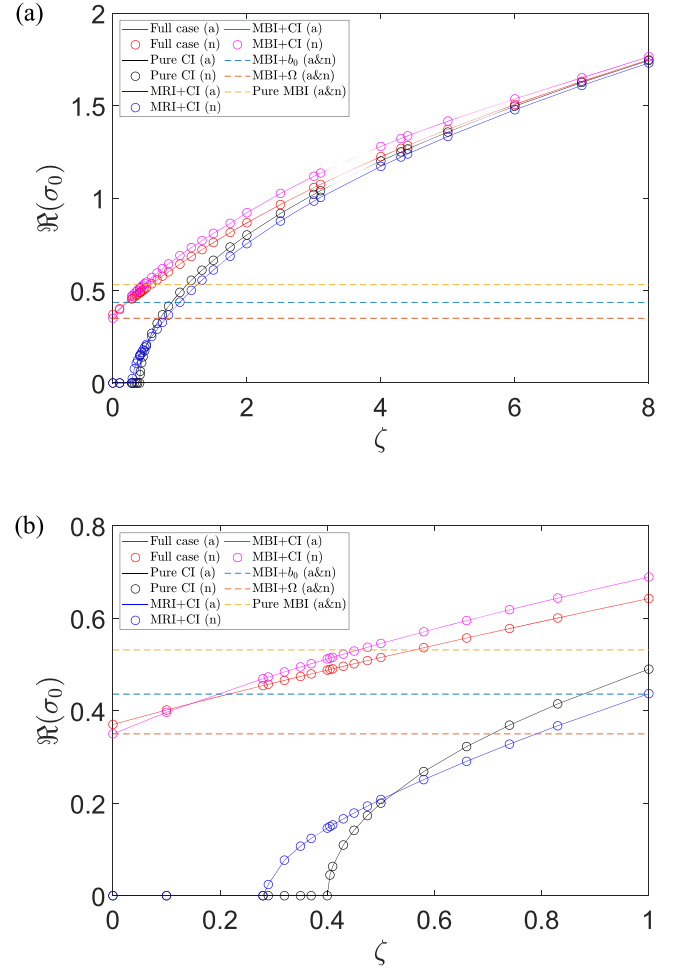


**Figure 5.** Positive branches of the real parts of the leading order growth rates of the most unstable modes of the full system and the various subcases, as a function of the basic shear flow gradient  $\zeta \in [0.0, 8.0]$  (upper plot) and  $\zeta \in [0.0, 1.0]$  (lower plot) for the strong-MBI case, defined by (42). The poloidal magnetic field has magnitude  $b_0 = 1/k$ . Analytic results (a) are represented by solid lines, numerical results (n) by circles. Dashed lines denote the shear-independent cases explained in the legend.

shear flow gradient  $\zeta$ , the instabilities in all the other subcases eventually become more unstable than any shear-independent case, owing to the presence of MRI and CI.

We now turn to the second set of parameter values given in (42), which describes the strong-MBI case. Figure 5 shows  $\sigma_0$ , calculated theoretically, and  $\sigma$ , calculated numerically from Equation (14), for the most unstable modes as a function of the shear flow gradient  $\zeta$ ; the upper plot covers the range  $0 < \zeta < 8$ , and the lower plot shows the range  $0 < \zeta < 1$  in more detail. As for the weak-MBI case, the dynamics for sufficiently strong shear gradients (here  $\zeta \gtrsim 8.0$ ) is eventually dominated by the CI for all subcases. However, for weaker shear, we again see that the different instability types require different minimum threshold values of  $\zeta$  to enter the dynamics. Similarly to the weak-MBI case, here it is also the pure CI for which the shear gradient threshold is highest ( $\zeta > 0.4$ ). A slightly lower value of  $\zeta$  ( $\zeta > 0.28$ ) is sufficient to excite the MRI. However, the system is now unstable even in the absence of a shear flow ( $\zeta = 0$ ) because of the relatively strong toroidal magnetic field gradient  $\lambda$ . It is also of note that, for any value of the shear gradient  $\zeta > 0.1$ , the greatest value of  $\sigma_0$  is observed for the subcase combining only the MBI and CI. Thus, for the strong-

MBI case, the introduction of a constant weak poloidal magnetic field  $b_0$  acts to stabilize the system (provided that the shear is not too weak). It can also be seen from Figure 5 that, on increasing the shear flow gradient  $\zeta$ , all the shear-dependent subcases eventually become more unstable than any of the shear-independent subcases, owing to the marked amplification of the MRI and CI with increasing  $\zeta$ .

#### 4. Next-order Asymptotic Analysis

The next-order analysis allows us to determine the potential evaluation points  $z_0$  for the most unstable eigenmode  $\tilde{w}(z)$  of Equation (14), as well as the leading order asymptotic approximation of such a solution, denoted by  $\tilde{w}_0(z)$ . As explained in Appendix C, the solution at zeroth order (the main flow, hereinafter MF) is simply  $w=0$ . The perturbation method reveals the strongly localized perturbations to this trivial solution. They can be classified into two categories: wall modes and body modes. Wall modes take the form of boundary layer solutions in which the evaluation points  $z_0$  lie on the boundaries of the domain; on one side, they satisfy the impermeability condition (15), and on the other, they match smoothly to the zero MF solution. Body modes, on the other hand, are internal layer-type solutions in which  $\Re(z_0)$  lies strictly inside the domain and that decay on both sides to zero. We now discuss the results for these two types of modes, with further details provided in Appendix D.

##### 4.1. Wall Modes

Wall modes are solutions  $\tilde{w}(z)$  of Equation (14) in the form of a boundary layer in the vicinity of the boundaries of the domain, either  $z_0=0$  or  $z_0=1$ , with the thickness of the boundary layer decreasing with increasing wavenumber  $k$ . This boundary layer thickness, denoted by  $\delta_1$ , scales with the value of  $k$  and by the relation (16) also with the value of the weak constant poloidal magnetic field  $b_0$ :

$$\delta_1 \sim k^{-2/3} \sim b_0^{2/3}. \quad (43)$$

It follows that the relation (43) establishes the vertical and horizontal spatial scales of the variations of interchange wall modes.

The leading order asymptotic approximation of the most unstable wall mode, which satisfies the impermeability condition  $\tilde{w}(z_0)=0$ , takes the form of an Airy function of the first kind (see formula (D10)):

$$\tilde{w}(z) \sim \tilde{w}_0(z) = \text{Ai} \left[ \chi_1 + k^{2/3}(z - z_0) \tilde{\Sigma}_z^{1/3} \right], \quad (44)$$

where  $\chi_1 \approx -2.338$  is the first zero of the Airy function, and where the complex number  $\tilde{\Sigma}_z$  is defined by (D4). Hence,  $\tilde{w}_0(z)$  is a complex function with the real and imaginary parts oscillating under the envelope of the function modulus  $|\tilde{w}_0(z)|$ . Selected plots of the wall modes are presented in Section 5.

It should be noted that in the subcases of the full problem related to the pure MBI or pure MRI, described in Section 3, the wall modes are approximated by the Airy function in a form similar to (44). However, in all these simpler unstable cases, the growth rate function  $\sigma(z)$  is a purely real positive function (at least on a part of the domain), and hence the growth rates  $\sigma$  are real numbers, and also the eigenmodes  $\tilde{w}(z)$  are purely real functions. For this reason, there could be at most one wall mode (when the growth rate function  $\sigma(z)$  is maximized at the

boundary of the domain) or none (when  $\sigma(z)$  is maximized strictly inside the layer). In the full system, however, the situation is different: owing to the complex form of Equation (17), the wall modes given by (44) always exist at both edges of the domain, provided that they are unstable, namely  $\Re(\sigma_0 = \sigma(z_0)) > 0$  at the evaluation points  $z_0=0$  or  $z_0=1$ . In addition, these complex solutions exhibit very strong oscillations in the real and imaginary parts, but still have a smooth Airy-type envelope  $|\tilde{w}_0(z)|$ . Finally, for the wall mode (44), the asymptotic approximation of the growth rate  $\sigma$ , including the first-order correction (D9), takes the form

$$\sigma = \sigma_0 - \left( |\chi_1| \tilde{\Sigma}_\sigma^{-1} \tilde{\Sigma}_z^{2/3} \right) k^{-2/3} + o(k^{-2/3}), \quad (45)$$

where  $\tilde{\Sigma}_\sigma$  is defined by (D4), and where  $k^{-2/3} \sim b_0^{2/3}$  from (43).

##### 4.2. Body Modes

For the pure MBI or pure MRI, described in Section 3,  $\sigma$  is real, and the body modes are the solutions  $\tilde{w}(z)$  of Equation (14) in the form of an internal layer confined strictly inside the domain in the vicinity of the evaluation point  $z_0$ , with  $0 < z_0 < 1$ . Outside this layer, the body mode decays exponentially to match the zero MF solution. The evaluation point  $z_0$  for the most unstable body mode is defined by the location where the growth rate function  $\sigma(z)$  has its global maximum inside the domain. More details of the analysis of the pure MBI case can be found in Mizerski et al. (2013).

However, for the full problem, the situation is more complicated, as described in detail in Appendix D. The leading order expression for the growth rate,  $\sigma_0$ , is now complex, and the evaluation point  $z_0$  is initially unknown. In other words, the growth rate function  $\sigma(z)$ , given implicitly by the equation  $W_0(z, \sigma) = 0$ , where  $W_0$  is defined by (A2c), is complex. It can then be shown—see Appendix D—that the condition for the existence of body modes is that the derivative of the growth rate function with respect to  $z$  has to vanish at the point  $z_0$ . This leads to a system of two algebraic equations for the unknown pair  $(z_0, \sigma_0)$ , i.e.,

$$0 = W_0(z_0, \sigma_0), \quad 0 = \frac{\partial}{\partial z} W_0(z, \sigma) \Big|_{(z, \sigma) = (z_0, \sigma_0)}. \quad (46)$$

The solution of the system (46) yields all allowed evaluation points  $z_0$  for the body modes and the leading order form of their growth rates  $\sigma_0$ . However, it turns out that (except in special cases) all  $z_0$  solutions are essentially complex, i.e.,  $\Im(z_0) \neq 0$ . Thus, significantly,  $\Re(z_0)$  is not, in general, the point where the function  $\Re(\sigma(z))$  has its maximum. Instead, the evaluation point  $z_0$  is a point where the complex- $z$  derivative of the growth rate function  $\sigma(z)$  is zero on the subdomain of the complex plane  $0 < \Re(z_0) < 1$  (Soward 1977; Soward & Jones 1983; Yano 1992; Jones et al. 2000). The asymptotic solution of Equation (14) is a complex-valued function  $\tilde{w}_0(z)$  of the real variable  $z$  with the associated complex eigenvalue  $\sigma$  at leading order equal to  $\sigma_0$ . Furthermore, the modulus, as well as the real and imaginary parts of the body modes  $\tilde{w}_0(z)$ , is not, in general, localized in the vicinity of the point  $\Re(z_0)$ , but rather about some other point  $0 < z_{\max} < 1$ , which we term the *localization point*. This fact has an important impact on the numerical search for solutions. Finally, it should be mentioned that, for

the pair  $(z_0, \sigma_0)$  satisfying Equations (46), the body mode does not necessarily have to exist, since additionally it has to fulfill the boundary conditions (15).

Next, the thickness of the internal layer-type body mode, denoted as  $\delta_2$ , needs to be established in terms of scaling with the value of  $k$  and, by the relation (16), also with the value of the weak constant poloidal wavenumber  $b_0$ . Similarly to Mizerski et al. (2013), and as explained in Appendix D,

$$\delta_2 \sim k^{-1/2} \sim b_0^{1/2}. \quad (47)$$

The relation (47) determines the vertical and horizontal spatial scales of variation of the interchange body modes.

The leading order asymptotic approximation of the most unstable body mode has the form of a complex Gaussian function (see Expression (D22)),

$$\tilde{w}(z) \sim \tilde{w}_0(z) = \exp\left[-\frac{1}{4}k(z - z_0)^2\tilde{\Upsilon}_z^{1/2}\right], \quad (48)$$

where  $\tilde{\Upsilon}_z$ , which is complex, is defined by Equation (D17). Hence,  $\tilde{w}_0(z)$  is a complex function with real and imaginary parts oscillating under the envelope of the function modulus  $|\tilde{w}_0(z)|$ . The modulus takes the shape of a Gaussian function of a real variable on the domain  $[0, 1]$ , localized near the localization point  $z_{\max}$ , which is determined by

$$z_{\max} = \Re(z_0) - \Im(z_0) \frac{\Im(\tilde{\Upsilon}_z^{1/2})}{\Re(\tilde{\Upsilon}_z^{1/2})}. \quad (49)$$

Expression (49) demonstrates clearly the difference between the evaluation point  $z_0$  and the localization point  $z_{\max}$ , i.e., the presence of the nonzero imaginary parts of  $z_0$  and  $\tilde{\Upsilon}_z$  (note that in the subcases related to the pure MBI or pure MRI,  $z_0$  and  $\tilde{\Upsilon}_z$  are both real, in which case  $z_{\max} = z_0$ ).

The eigenmode approximation  $\tilde{w}_0(z)$  given by (48) has the same structure as the body modes in the case of the pure MBI (see Mizerski et al. 2013) as well as in the case of the MBI with magnetic diffusion (see Gradzki & Mizerski 2018). In the latter case, the weak magnetic diffusivity plays a similar role to that of the weak poloidal field  $b_0$  in the current study, namely establishing the horizontal and vertical length scales of variation of the most unstable perturbation. Finally, for a body mode given by (48), the asymptotic approximation of the growth rate  $\sigma$  up to first order takes the form

$$\sigma = \sigma_0 - \left(\frac{1}{2}\tilde{\Upsilon}_\sigma^{-1}\tilde{\Upsilon}_z^{1/2}\right)k^{-1} + o(k^{-1}), \quad (50)$$

where  $\tilde{\Upsilon}_\sigma$ , which is complex, is defined by Equation (D19), and  $k^{-1} \sim b_0$  from the relation (47).

## 5. Numerical Solutions of the Full System

The linear stability to interchange modes of the system under consideration is governed, in general, by the second-order ordinary differential equation (14) for  $\tilde{w}(z)$ , the amplitude of the vertical velocity perturbation; the growth rate  $\sigma$  is determined as the eigenvalue. In Sections 3 and 4, we considered the high-wavenumber limit ( $k \gg 1$ ), thereby allowing analytical progress in determining both the growth rate and spatial structure of the unstable modes. Here, we present numerical solutions of Equation (14), with boundary conditions

(15), and compare these with the corresponding analytical expressions from Sections 3 and 4.

In Section 3.5, we presented numerical results for subcases of the full system, with at least one of the main physical ingredients neglected. In this section, we utilize the same two representative sets of parameter values: Set (41), which we refer to as the *weak-MBI* case, and Set (42), which we refer to as the *strong-MBI* case. However, contrary to the approach of Section 3.5, here we present the results for certain fixed values of the shear gradient  $\zeta$ , so as to focus on verification of the analytical results from Section 4, together with identification of the most unstable mode. In this section, we treat the poloidal magnetic field  $b_0$  as a constant, although we consider different values of  $b_0$ . Recall that in the theoretical analysis of Sections 3 and 4, we adopted the ordering  $b_0 \sim 1/k$ ; it is therefore important to examine the validity of this assumption by investigating cases in which  $b_0$  is fixed, and we explore, numerically, a wide range of wavenumbers  $k$ . To solve Equation (14) numerically, we utilize the MATLAB `bvp4c` function for the solution of boundary value problems. The solver employs a finite difference routine that implements the three-stage, fourth-order Lobatto IIIa implicit method (for details, see Shampine & Kierzenka 2001). Since we are considering interchange solutions, with transverse wavenumber  $k$ , we seek to maximize the eigenvalue  $\sigma$  over all positive  $k$ , for a chosen basic state and a fixed set of nondimensional parameters of the system, in particular the weak constant poloidal magnetic field  $b_0$ .

In Section 5.1, for the weak-MBI case, and Section 5.2, for the strong-MBI case, we present a comparison of the analytical and numerical results. We consider three representative values of the negative shear flow gradient, leading to three distinct cases: CI-stable (with  $\kappa^2 > 0$ ), CI-neutral ( $\kappa^2 = 0$ ), and CI-unstable ( $\kappa^2 < 0$ ). Initially, we focus on one selected value for the magnitude of the weak poloidal field, namely  $b_0 = 10^{-4}$ ; under assumption (16), we thus anticipate the wavenumbers of the most unstable modes of  $O(10^4)$ . For this value of  $b_0$ , we show the analytically and numerically obtained dispersion relations  $\sigma(k)$  for the three cases of  $\kappa^2 > 0$ ,  $\kappa^2 = 0$ , and  $\kappa^2 < 0$ . We then present each of the three cases separately, together with the dispersion relations for all the subcases described in Section 3. This makes it possible to observe which of the physical ingredients has a stabilizing or destabilizing effect on the flow and how they affect the full system. We then focus on the most interesting situation ( $\kappa^2 = 0$ ), in which only the MBI and MRI compete at leading order. For the most unstable modes, we show the eigenmode solutions of Equation (14) and the scaling relation  $k(b_0)$  for a wide range of poloidal field strengths, with  $b_0$  ranging from  $10^{-1}$  to  $10^{-10}$ .

### 5.1. Weak-MBI Case

The weak-MBI case is defined by the physical parameters (41), namely

$$\begin{aligned} \mathcal{P} &= 1.9, \quad \alpha = 1.0, \quad \Lambda = 0.2, \\ \lambda &= 1.35, \quad \mathcal{U}_u = 1.0, \quad \mathcal{U}_\Omega = 1.0, \end{aligned} \quad (51)$$

together with a linear basic-state toroidal magnetic field  $a_0(z) = 1 + \lambda(1 - z)$ , a basic-state shear flow  $u_0(z) = -\zeta z$  ( $\zeta > 0$ ), and the strength  $b_0$  of the uniform poloidal field. As noted earlier, for such a setup in the absence of any shear flow ( $\zeta = 0$ ), the MBI is completely suppressed by rotation, regardless of the

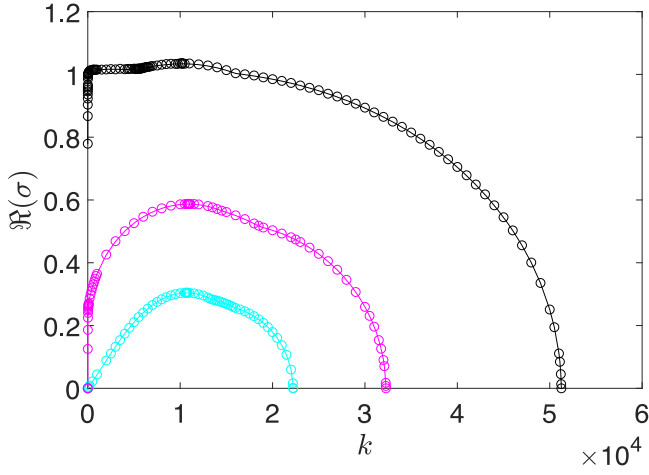


**Figure 6.**  $\Re(\sigma(k))$  as a function of  $k$  for the weak-MBI case, with  $b_0 = 10^{-4}$ . Solid lines and circles respectively denote the analytically and numerically determined values of  $\sigma$ :  $\zeta = 0.5$  (cyan,  $\kappa^2 > 0$ );  $\zeta = 1.0$  (magenta,  $\kappa^2 = 0$ );  $\zeta = 2.0$  (black,  $\kappa^2 < 0$ ).

presence of the poloidal field. Hence, we can expect that, in this case, the major role is played by the MRI (for moderate values of  $\zeta$ ) or the CI (for sufficiently strong  $\zeta$ ). We may then ask how the MRI and CI are affected by the presence of the toroidal magnetic field  $a_0(z)$ .

Figure 6 shows the growth rates—calculated both analytically and numerically—as a function of wavenumber for a uniform poloidal magnetic field  $b_0 = 10^{-4}$ , and for three values of  $\zeta$  (leading to the three cases in  $\kappa^2$ ). In all cases, the dispersion relation has a clear global maximum around  $k \approx 10^4$ ; importantly, the preferred wavenumber, calculated numerically without any prior assumption, is in line with our assumed theoretical scaling  $k \sim b_0^{-1}$ . The influence of the basic shear flow gradient  $\zeta$  is also clearly visible. Greater values of  $\zeta$  make the instability more vigorous since the shear amplifies both the MRI and CI (see Expressions (18) and (26)). Increasing  $\zeta$  also enhances the instability on wavelengths longer than that of the most unstable mode, reflecting the fact that, for sufficiently large shear, the system is dominated by the CI, the growth rate of which is independent of wavenumber at leading order.

Figure 7 shows separately the growth rates as functions of  $k$  for the three cases of Figure 6, together with the relevant subcases. For the subcases with no poloidal field (namely MBI, CI, and MBI+CI), the growth rate at leading order  $\sigma_0$  is independent of wavenumber. We can see that the full weak-MBI case is always more unstable than the relevant subcases (i.e., those including the basic shear flow and rotation). Thus, incorporation of the basic-state toroidal field  $a_0(z)$  into the system enhances the instability from the MRI+CI subcase, regardless of whether or not the system is stable with respect to the CI. This is not an obvious result, especially in the CI-stable case (Figure 7(a)), in which the rotation is strong enough to suppress the pure MBI completely, but the vertical Coriolis force is too weak to destabilize the toroidal magnetic field  $a_0(z)$  itself (see Expression (27)). Furthermore, incorporation of the toroidal field modifies the shape of the function  $\Re(\sigma(k))$ , making its global maximum more prominent. On the other hand, with increasing shear flow gradient  $\zeta$ , the nature of the instability of the full system becomes similar to the MRI+CI subcase, with the growth rate  $\sigma_0$  tending to the value of the CI, MRI+CI, and MBI+CI subcases. As the shear increases,  $\kappa^2$

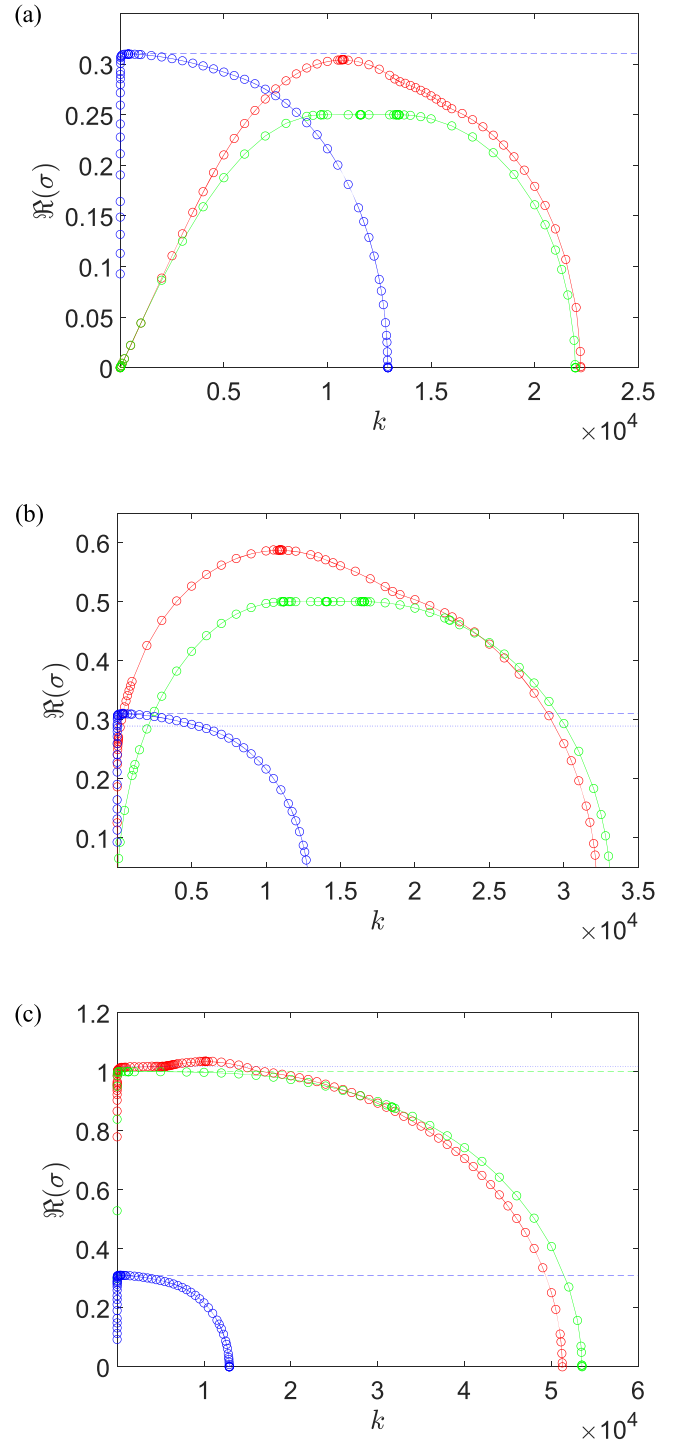


**Figure 7.**  $\Re(\sigma(k))$  as a function of  $k$ : a comparison between the full weak-MBI case (red) and its subcases (green and blue), with constant poloidal magnetic field  $b_0 = 10^{-4}$ : (a)  $\zeta = 0.5$ ,  $\kappa^2 > 0$ ; (b)  $\zeta = 1.0$ ,  $\kappa^2 = 0$ ; (c)  $\zeta = 2.0$ ,  $\kappa^2 < 0$ . Analytically and numerically determined growth rates  $\sigma$  are denoted by solid lines and circles respectively. The blue and green solid lines and circles correspond respectively to the MBI+ $b_0$  and MRI+CI subcases. The horizontal lines indicate the  $k \rightarrow \infty$  limit of the following subcases: pure MBI (blue dashed line), MBI+CI (blue dotted line) and pure CI (green dashed line).

decreases (becoming more negative; see Expressions (21) and (27)), and hence, the purely hydrodynamic effect of rotation dominates over all magnetic factors.

Finally, we focus on the situation with  $\kappa^2 = 0$  ( $\zeta = 1.0$ ), where, at leading order of the full weak-MBI case, only the

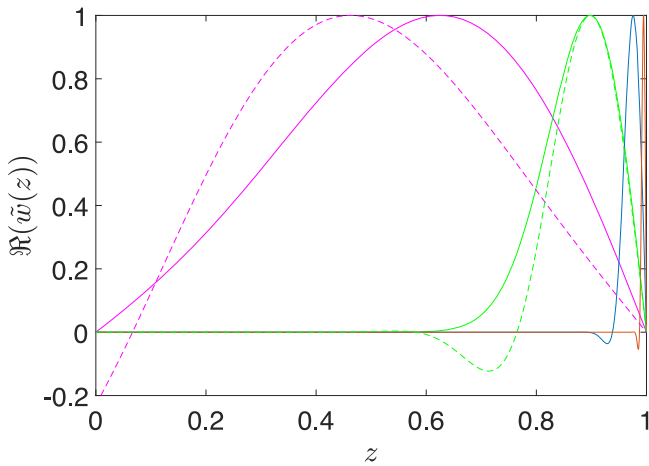


**Figure 8.** Real parts of the analytic (dashed lines) and numerical (solid lines) solutions for the most unstable eigenmodes  $\Re(\tilde{w}(z))$  for  $b_0 = 10^{-1}$  ( $k = 14$ ; magenta),  $b_0 = 10^{-2}$  ( $k = 115$ ; green),  $b_0 = 10^{-3}$  ( $k = 1100$ ; blue),  $b_0 = 10^{-4}$  ( $k = 10890$ ; red). The plots correspond to the full weak-MBI case that is neutrally stable with respect to the pure CI ( $\kappa^2 = 0$ ). For  $b_0 \leq 10^{-3}$ , the analytical and numerical results are indistinguishable.

MBI and MRI come into play. For  $b_0 = 10^{-4}$ , the dispersion relation is presented in Figure 7(b). A more detailed study, covering a wide range of values of  $b_0$ , reveals that the most unstable mode  $\tilde{w}(z)$  is always a wall mode localized near the top of the layer. Hence, it can be approximated by a complex Airy function of the first kind, given by (44), with  $z_0 = 1$ . Figure 8 shows the real parts of the eigenfunctions  $\tilde{w}(z)$  for four different values of the poloidal magnetic field strength:  $b_0 = 10^{-1}$ ,  $10^{-2}$ ,  $10^{-3}$ , and  $10^{-4}$ . Since our theoretical results are obtained under the asymptotic assumptions of short-wavelength modes ( $k \gg 1$ ) and a weak magnetic field ( $b_0 \ll 1$ , with  $b_0 \sim 1/k$ ), it is clear that the agreement between the theoretical and numerical results must increase with decreasing  $b_0$ . As can be seen from Figure 8, for  $b_0 = 10^{-1}$  (for which the preferred wavenumber is  $k = 14$ ), the agreement is relatively poor, whereas for  $b_0 = 10^{-2}$  ( $k = 115$ ), the location of the maximum of the eigenfunction (although not its entire spatial extent) is well captured by the asymptotic approach. For  $b_0 = 10^{-3}$  ( $k = 1100$ ) and even weaker poloidal fields, the analytic and numerical results are indistinguishable. With decreasing  $b_0$  (and hence increasing wavenumber  $k$ ), the eigenmodes become more and more localized near the upper boundary of the layer, in agreement with the results of Mizerski et al. (2013) and Gradzki & Mizerski (2018) for the case of the pure MBI.

The agreement between the analytic and numerical results validates not only the asymptotic assumptions of  $k \gg 1$  and  $b_0 \ll 1$  but also, significantly, the assumed scaling  $k \sim b_0^{-1}$  for the wavenumber of the most unstable mode. Figure 9 plots the wavenumber of the most unstable mode versus  $b_0$  for the range  $10^{-10} < b_0 < 10^{-1}$ . The red solid line shows the preferred wavenumber obtained analytically, by maximizing Expressions (45) and (50) with respect to the wavenumber  $k$ , having identified the localization point  $z_0$  and determined the preference between wall and body modes for each  $k$ . The slope of the red line is very close to  $-1$ ; more precisely the red line can be described by the fit  $k = C_w(b_0)b_0^{-1}$ , where the coefficient  $C_w(b_0) = 1.24b_0^{0.008}$ . Note that the scaling holds over a wide range of  $b_0$ ; from relatively long “short waves,” with  $k \sim 10$  (and relatively strong “weak poloidal field”

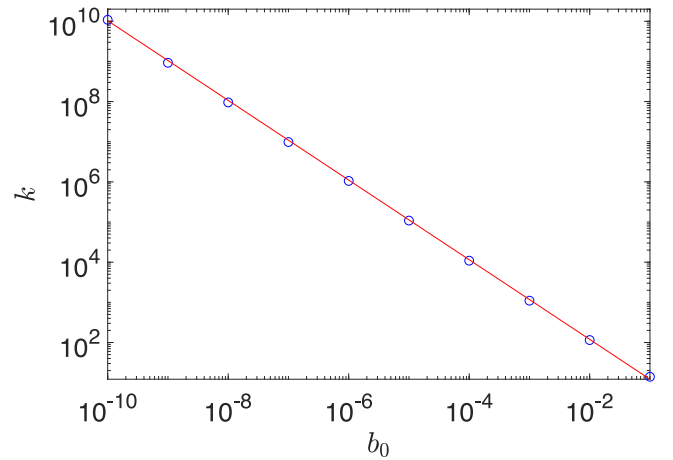


**Figure 9.** Wavenumber  $k$  of the most unstable mode as a function of  $b_0$  for the full weak-MBI case with  $\kappa^2 = 0$ . The blue circles are calculated numerically from the full system (14). The red solid line is obtained analytically from Equations (45) and (50).

$b_0 \sim 0.1$ ), to very high values of  $k$  (and accordingly weak  $b_0$ )—modes that would probably no longer be physically significant, owing to diffusion. Thus the scaling  $k \sim b_0^{-1}$  for the wavenumber of the most unstable mode is satisfied for the entire physically significant range of values of the weak constant field  $b_0$  (see Figures 2(b), 4(b), and 6(b) in Gradzki & Mizerski 2018, for a similar relationship between  $k$  and diffusivities).

## 5.2. Strong-MBI Case

We now turn to the strong-MBI case, defined by parameter set (42), namely

$$\begin{aligned} \mathcal{P} &= 1.9, \quad \alpha = 1.0, \quad \Lambda = 0.2, \\ \lambda &= 1.95, \quad \mathcal{U}_u = 1.0, \quad \mathcal{U}_\Omega = 0.4, \end{aligned} \quad (52)$$

together with a linear basic-state toroidal magnetic field  $a_0(z) = 1 + \lambda(1 - z)$ , a basic-state shear flow  $u_0(z) = -\zeta z$  ( $\zeta > 0$ ), and the value of the weak uniform poloidal magnetic field  $b_0$ . For such a setup, and in contrast to the weak-MBI case, the MBI is not suppressed by rotation, regardless of the presence of the poloidal field  $b_0$  or the shear flow  $u_0(z)$ . Hence, in this case, we can expect a coupling between the MBI and MRI (for relatively moderate values of  $\zeta$ ) and between the MBI and CI (for sufficiently large  $\zeta$ ).

Figure 10 shows the growth rates, obtained analytically and numerically, as a function of wavenumber, for a uniform poloidal magnetic field  $b_0 = 10^{-4}$  and for three values of  $\zeta$  (leading again to the three cases in  $\kappa^2$ ). In all the cases, the dispersion relation  $\sigma(k)$  has a distinct global maximum for  $k \sim 10^4$ , and hence in line with our assumed theoretical asymptotic scaling  $k \sim b_0^{-1}$ . Again, greater values of  $\zeta$  enhance the instability through amplification of the MRI and the CI (see Expressions (18) and (26)), but also indirectly by amplification of the MBI (Expression (27)). As the shear is increased, the mode of maximum growth rate assumes a smaller wavenumber, which is accompanied by a broadening of the maximum. For sufficiently large shear (strongly negative  $\kappa^2$ ), the system is dominated by the CI (which is dispersionless at leading order).

Figure 11 shows separately the growth rates versus  $k$  for the three cases of Figure 10, together with the relevant subcases. For all the subcases with no poloidal magnetic field (i.e., MBI,

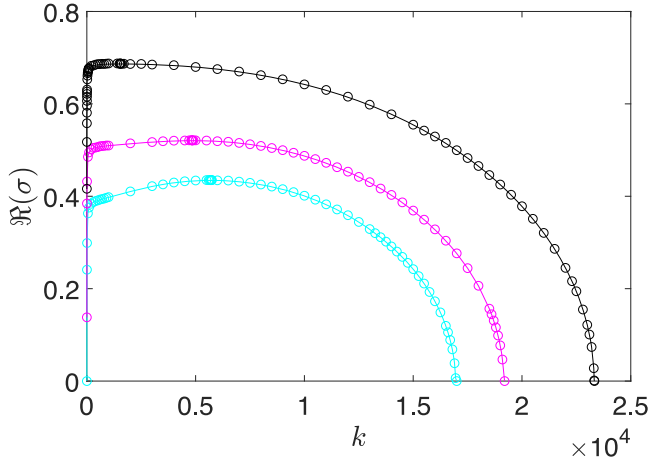


**Figure 10.**  $\Re(\sigma(k))$  as a function of  $k$  for the strong-MBI case, with  $b_0 = 10^{-4}$ . Solid lines and circles respectively denote the analytically and numerically determined values of  $\sigma$ :  $\zeta = 0.1$  (cyan,  $\kappa^2 > 0$ );  $\zeta = 0.4$  (magenta,  $\kappa^2 = 0$ );  $\zeta = 1.0$  (black,  $\kappa^2 < 0$ ).

CI, MBI+CI, and MBI+ $\mathcal{U}_\Omega$ ), the leading order growth rate  $\sigma_0$  is independent of wavenumber. It can be seen that the full strong-MBI case is always more unstable than the relevant subcases; i.e., those including the effects of the basic-state shear flow and rotation. Thus, the incorporation of a toroidal magnetic field  $a_0(z)$  enhances the instability from the MRI+CI subcase (green solid line and circles) regardless of whether the system is stable ( $\kappa^2 \geq 0$ ) or not ( $\kappa^2 < 0$ ) with respect to the CI alone (green dashed line). The amplification is clearly stronger than that in the weak-MBI case shown in Figure 7, since here the MBI is more vigorous. On the other hand, for shear flow gradient  $\zeta = 1.0$ , the maximum growth rate  $\sigma$  of the full system, corresponding to a fixed wavenumber  $k$ , is nearly the same as the leading order value  $\sigma_0$  of the MBI+CI subcase (where  $b_0 = 0$ ; Figure 11(c)). This shows the domination of the MBI in the strong-MBI case. For very strong shear gradients, i.e.,  $\zeta \gg 1$ , the system, as expected, eventually becomes dominated by the CI-like instability.

Finally, we focus on the situation when  $\kappa^2 = 0$  (i.e.,  $\zeta = 0.4$ ), in which, at leading order, the full strong-MBI case contains interactions between only the MBI and MRI; the dispersion relation for this case, for  $b_0 = 10^{-4}$ , is presented in Figure 11(b). A study covering a wide range of values of poloidal field strength  $b_0$  reveals that the most unstable mode  $\tilde{w}(z)$  is always a wall mode localized near the bottom of the layer. It can thus be approximated by a complex Airy function of the first kind, given by Expression (44) for  $z_0 = 0$ ; the eigenfunctions are plotted in Figure 12, for  $b_0 = 10^{-1}$ ,  $10^{-2}$ ,  $10^{-3}$ , and  $10^{-4}$ . As described above for the weak-MBI case, the agreement between theoretical and numerical results must increase with decreasing  $b_0$ . For  $b_0 = 10^{-1}$  (for which the wavenumber of the most unstable mode is  $k = 8$ ), the agreement is relatively poor; for  $b_0 = 10^{-2}$  ( $k = 59$ ), the location of the maximum of the eigenmode is correctly predicted by the analytical result (green dashed line); for yet weaker poloidal fields ( $b_0 \lesssim 10^{-3}$ ), the analytic and numerical results over all  $z$  are indistinguishable. With decreasing  $b_0$  (and hence increasing wavenumber  $k$ ), the eigenmodes become more and more localized near the upper boundary of the layer, in agreement with the results of Mizerski et al. (2013) and Gradzki & Mizerski (2018) for the case of the pure MBI.

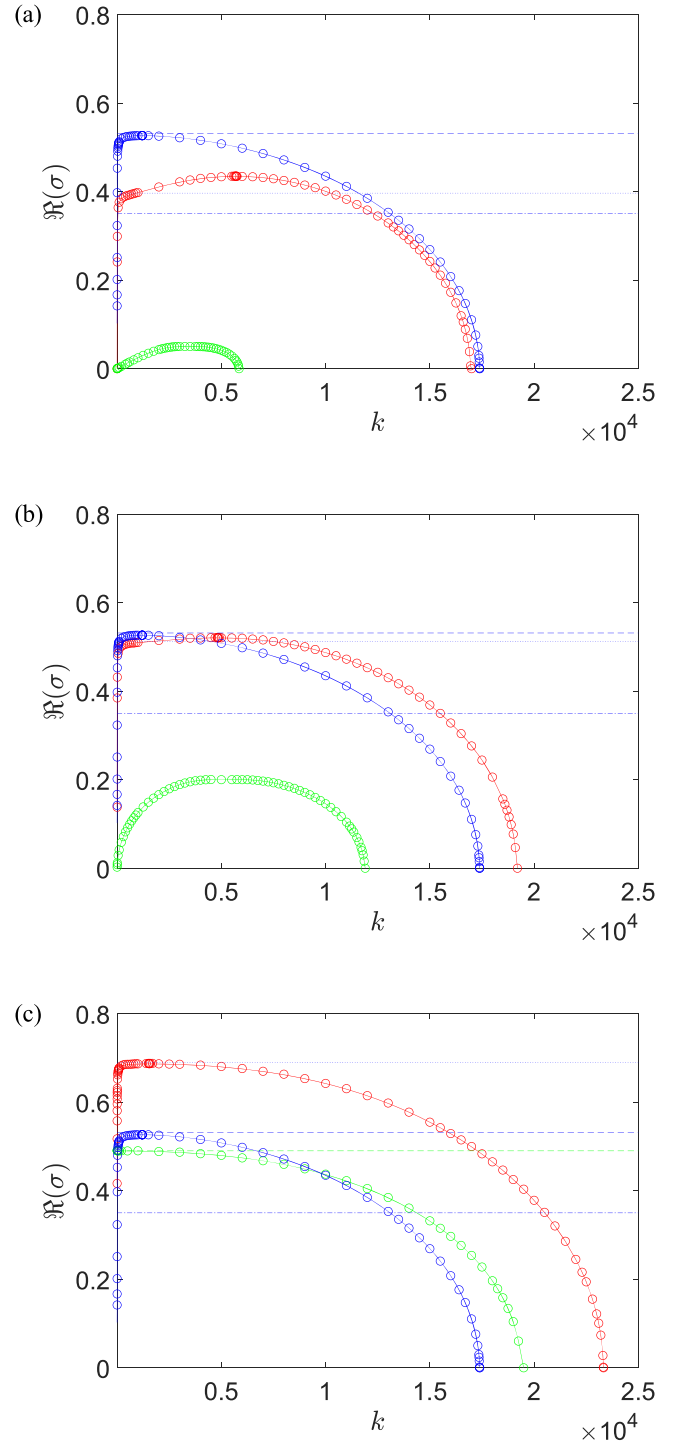


**Figure 11.**  $\Re(\sigma(k))$  as a function of  $k$ : a comparison between the full strong-MBI case (red) and its subcases (green and blue), with constant poloidal magnetic field  $b_0 = 10^{-4}$ : (a)  $\zeta = 0.1$ ,  $\kappa^2 > 0$ ; (b)  $\zeta = 0.4$ ,  $\kappa^2 = 0$ ; (c)  $\zeta = 1.0$ ,  $\kappa^2 < 0$ . Analytically and numerically determined growth rates  $\sigma$  are denoted by solid lines and circles respectively. The blue and green solid lines and circles correspond respectively to the MBI+ $b_0$  and MRI+CI subcases. The horizontal lines indicate the  $k \rightarrow \infty$  limit of the following subcases: pure MBI (blue dashed line), MBI+ $\mathcal{U}_\Omega$  (blue dotted-dashed line), MBI+CI (blue dotted line) and pure CI (green dashed line).

Figure 13 shows that, as for the weak-MBI case, the scaling  $k \sim b_0^{-1}$  is again valid; in this case, the red line can be described by  $k \approx C_s(b_0)b_0^{-1}$ , where the coefficient  $C_s(b_0) \approx 0.654b_0^{0.019}$ .

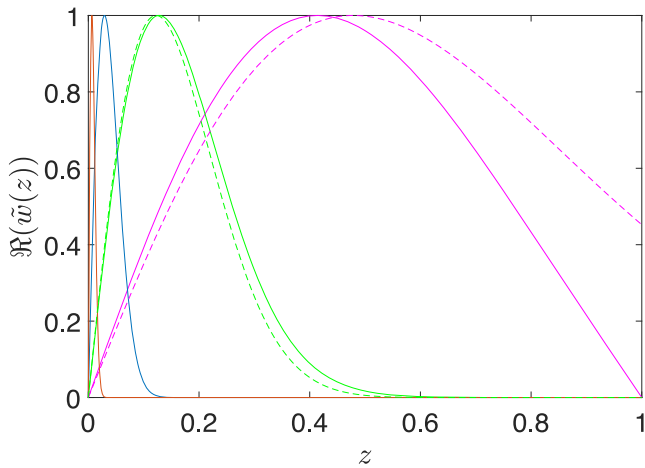


**Figure 12.** Real parts of the analytic (dashed lines) and numerical (solid lines) solutions for the most unstable eigenmodes  $\Re(\tilde{w}(z))$  for  $b_0 = 10^{-1}$  ( $k = 8$ ; magenta),  $b_0 = 10^{-2}$  ( $k = 59$ ; green),  $b_0 = 10^{-3}$  ( $k = 510$ ; blue),  $b_0 = 10^{-4}$  ( $k = 4840$ ; red). The plots correspond to the full strong-MBI case that is neutrally stable with respect to the pure CI ( $\kappa^2 = 0$ ). For  $b_0 \leq 10^{-3}$ , the analytical and numerical results are indistinguishable.

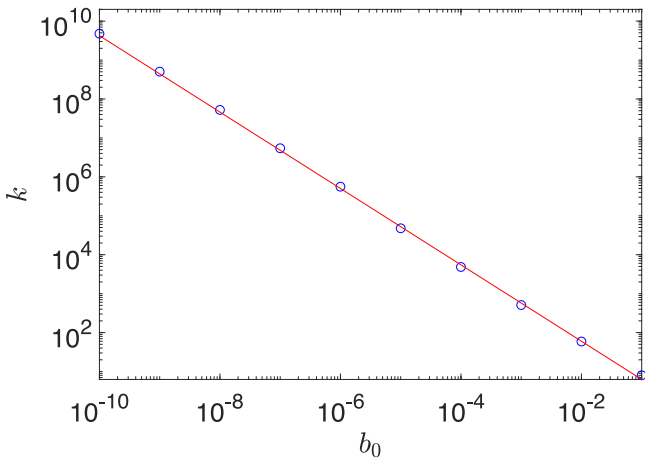


**Figure 13.** Wavenumber  $k$  of the most unstable mode as a function of  $b_0$  for the full strong-MBI case with  $\kappa^2 = 0$ . The blue circles are calculated numerically from the full system (14). The red solid line is obtained analytically from Equations (45) and (50).

## 6. Discussion

We have investigated the linear stability of an isothermal, electrically perfectly conducting, inviscid, perfect gas, with respect to interchange (or axisymmetric) modes. The joint action of gravity, background rotation, and velocity shear, together with height-dependent toroidal and constant poloidal components of the basic-state magnetic field, results in a coupling—which could be either cooperative or competitive—between centrifugal (CI), magnetorotational (MRI), and magnetic buoyancy (MBI) instabilities. Incorporating the poloidal field is a novel aspect of our analysis compared to previous studies, such as those of Acheson (1978) and Gilman (2018a, 2018b). The linear perturbation equations may be reduced to a second-order boundary value problem, in the form of Equation (14) and boundary conditions (15), with the growth rate appearing as the eigenvalue. Physically, the preferred modes have a large transverse horizontal wavenumber  $k$ . We are able to exploit the ordering  $k \gg 1$  to tackle the problem

analytically via a Rayleigh–Schrödinger perturbation approach; in order to bring the uniform constant poloidal magnetic field into play, we furthermore assume that its magnitude  $b_0 = O(k^{-1})$ . To aid with the understanding of the full system, which is quite complicated, we have also considered various subcases, comprising either the individual components of CI, MRI, and MBI or specific combinations of these. To complement our analytical approach, we have also solved the governing boundary value problem numerically, with no a priori assumption on the magnitude of  $k$  or  $b_0$ ; agreement between the analytical and numerical approaches is very good.

A consequence of the modes possessing a large horizontal wavenumber  $k$  is that they are strongly localized in the vertical direction. The leading order (in  $k^{-1}$ ) of the perturbation analysis yields Equation (17), the “depth-dependent dispersion relation,” which provides the leading order approximation to the growth rates. Determining the form of the eigenfunctions comes at the next order, through establishing the nature of their localization; in simple subcases, the localization point  $z_0$  is real, although, in general, it is complex. The localized solutions take the form of either wall modes (described by Airy functions) or body modes (described by parabolic cylinder functions). The presence of the weak constant poloidal field  $b_0$  establishes a finite wavenumber of the most unstable mode. This effect is qualitatively similar to that caused by the presence of diffusion in the system. We have established that the horizontal wavenumber  $k$  of the most unstable mode scales with the poloidal magnetic field  $b_0$  as  $k \sim b_0^{-1}$ . Moreover, the vertical scale of the most unstable mode (the thickness  $\delta$  of the internal and/or boundary layer) depends on the type of mode (i.e., on its localization point):  $\delta \sim k^{-2/3} \sim b_0^{2/3}$  for wall modes and  $\delta_1 \sim k^{-1/2} \sim b_0^{1/2}$  for body modes.

The epicyclic frequency  $\kappa$  is a convenient indicator of the presence of either the CI in the system ( $\kappa^2 < 0$ ) or the stabilizing nonmagnetic effect of rotation ( $\kappa^2 > 0$ ). Increasing the shear gradient preferentially amplifies modes with wavelength longer than that of the most unstable mode, leading to a flattening of the  $\sigma(k)$  curve, as shown in Figures 6 and 10. The MRI is always present in the full system for any nonzero shear flow no matter how weak, and it is in general amplified by the toroidal magnetic field. The most general case, when all three instability types interact (MBI+MRI+CI) seems to be always more unstable than any subcase that involves the shear flow and rotation: MBI+CI, MRI+CI, or pure CI. The pure MBI is always stabilized by background rotation; however, in the presence of a shear flow, the MBI can be amplified by the Coriolis force (which contributes to the effective gravity) through the coupling with the vigorous CI, if the shear flow gradient is sufficiently strong. It is also of interest to note that, for the case of MBI+ $b_0$ , the poloidal field can, in certain situations, amplify an existing MBI, or even destabilize a system that is stable to MBI.

It is natural to ask how our findings relate to the Sun, and, in particular, the solar tachocline—the thin region of velocity shear (both radial and latitudinal) sandwiched between the convective and radiative zones. In many models of the solar dynamo, it is postulated that the toroidal magnetic field is generated by the shearing motions within the tachocline. It is generally assumed that MBI is the primary mechanism for the release of magnetic field from the tachocline into the overlying convection zone (see Hughes 2007). It is therefore of particular interest to investigate what additional role may also be played

by CI or MRI. From the parameter values in Hughes et al. (2007), we may estimate the rotation parameter to be  $U_\Omega \sim 10^{-4}$  and the shear flow gradient to be  $\zeta \sim 10^{-1}$  (calculated as  $\zeta = d\Delta U / U_s \Delta z$ , where  $d = 3.5 \times 10^4$  km is the thickness of the tachocline,  $U_s = 1.4326$  km s $^{-1}$  is the velocity scale, and  $\Delta U / \Delta z = \Delta U / (0.04 \times R_\odot) = 4.14062 \times 10^{-6}$  s $^{-1}$  is the mean shear rate). Hence, assuming a linear basic shear flow  $u_0(z) = -\zeta z$ , the squared epicyclic frequency given by Expression (19) is negative and small in magnitude ( $-\kappa^2 \sim 10^{-7}$ ). It follows therefore that any CI in the tachocline will be weak ( $\sigma_{\text{CI}} \sim 10^{-4}$ ). If, as noted above, the MBI is the primary instability mechanism operative in the tachocline, then, at least in a qualitative sense, it is what we have called the *strong-MBI case* that will be relevant in this context. A key result of our analysis is that even a weak poloidal field can play a major role in determining the scale of the instabilities. However, the magnitude of the poloidal magnetic field in the tachocline is highly uncertain. Estimates of the strength of the poloidal field range from very weak values of  $O(10^{-4}$  G) (Gough 2007) to relatively strong values of  $O(10^3$  G) (e.g., Forgács-Dajka & Petrovay 2002). In dimensionless terms, this considerable extent of possible poloidal field strengths corresponds to the range  $10^{-9} < b_0 < 10^{-2}$ . It follows therefore, from the scaling  $k \sim b_0^{-1}$ , that the wide range of  $b_0$  would establish a correspondingly wide range of transverse ( $y$ ) wavelengths of the most unstable modes: from the rather unphysical 1 m through to  $10^4$  km, which is of the order of the thickness of the tachocline. Although very small wavelengths will be damped by diffusion (see, e.g., the estimates in Gradzki & Mizerski 2018), the theoretical relationship between  $b_0$  and the transverse scale of the instability could be a useful tool in pinning down the strength of the poloidal field in the tachocline. It is of interest to estimate the strength of the poloidal field at which the length scale set by the poloidal field is comparable with the length scale set by diffusive considerations. Gradzki & Mizerski (2018) provide an estimate of the most unstable wavelength in the solar tachocline, based on diffusive considerations, of  $\lambda \approx 10^2$  km. The corresponding value of the wavenumber  $2\pi \times 10^{-5}$  m $^{-1}$ , with the use of the relation  $kb_0 \approx 1$  (dimensionally  $kb_0 = B_s/d$ , with  $B_s \approx 100$  kG

being an estimate of the toroidal field strength in the tachocline), would lead to the following estimate of the magnitude of the poloidal field in the solar tachocline:  $b_0 \approx 50$  G.

The results described here suggest a number of possible extensions of our model. Within linear theory, it would be interesting (although decidedly nontrivial) to consider three-dimensional (“undular”) disturbances, as did Mizerski et al. (2013) for the pure MBI, as well as the effects of diffusion, as did Gradzki & Mizerski (2018), also for the pure MBI. In a complementary approach, it would be of interest to consider the influence of a poloidal field in the spherical geometry model studied by Gilman (2018a, 2018b). Of particular interest would be to investigate the combined influence of the various instabilities in the nonlinear regime. Cattaneo et al. (1990) studied the nonlinear evolution of pure MBI of a basic-state magnetic field with both toroidal and poloidal components, but without the effects of rotation or velocity shear. Vasil & Brummell (2008) and Silvers et al. (2009) considered the nonlinear evolution of MBI arising from the shearing of a weak vertical magnetic field by a horizontal velocity shear, but without the effects of rotation or the horizontal poloidal component of field. Brandenburg & Schmitt (1998), Wissink et al. (2000), and Chatterjee et al. (2011) investigated the nonlinear evolution of a purely toroidal magnetic field, including the effects of rotation, with particular emphasis on calculating the resulting mean-field  $\alpha$ -effect. Putting all of the ingredients together in a tractable computational model would be an important next step toward fully understanding the instabilities of the tachocline.

### Acknowledgments

This work was financed by the National Science Centre, Poland (grant No. 2019/32/C/ST3/00482). D.W.H. would like to thank the Isaac Newton Institute for Mathematical Sciences, Cambridge, for support and hospitality during the programme DYT2, where some of the writing of the paper was undertaken. This work was supported by EPSRC grant No. EP/R014604/1.

## Appendix A The Coefficients of Equation (15)

The coefficients of the governing ordinary differential Equation (14) take the general form:

$$\widetilde{W}_2(z) = -k^{-2}W_2(z) + \mathcal{O}(k^{-4}; k^{-2}b_0^2; b_0^4; k^2b_0^6), \quad (\text{A1a})$$

$$\widetilde{W}_1(z) = -k^{-2}W_1(z) + \mathcal{O}(k^{-4}; k^{-2}b_0^2; b_0^4), \quad (\text{A1b})$$

$$\widetilde{W}_0(z) = W_0(z) + \mathcal{O}(k^{-2}; k^4b_0^6; k^2b_0^4; kb_0^3; b_0^2; k^{-1}b_0), \quad (\text{A1c})$$

where the functions  $W_2(z)$ ,  $W_1(z)$ , and  $W_0(z)$  are of order unity, and are given by

$$W_2(z) = \left(k^2b_0^2\Lambda + \sigma^2\rho_0(z)\right)\left(k^2b_0^2\Lambda\mathcal{P}\alpha + \sigma^2F(z)\right), \quad (\text{A2a})$$

$$W_1(z) = \sigma^2(k^2b_0^2\Lambda\mathcal{P}\alpha + \sigma^2F(z))D\rho_0(z), \quad (\text{A2b})$$

$$W_0(z) = A_4(z)\sigma^4 + A_2(z)\sigma^2 + A_1(z)\sigma + A_0(z). \quad (\text{A2c})$$

The functions  $A_j(z)$  are functions of the basic state that do not contain terms involving either  $k$  or  $b_0$  alone, only terms proportional to  $k^j b_0^j \sim 1$  for  $j = 1, 2, 4$ . Specifically,

$$A_4(z) = \rho_0 F = \rho_0(\Lambda a_0^2 + \mathcal{P}\alpha\rho_0), \quad (\text{A3a})$$

$$A_2(z) = k^2b_0^2\Lambda(F + \mathcal{P}\alpha\rho_0) - \Lambda a_0^2\rho_0(f - \mathcal{U}_\Omega\mathcal{U}_u u_0)(H_\rho^{-1} - H_B^{-1}) + \mathcal{U}_\Omega\rho_0 F(\mathcal{U}_\Omega + \mathcal{U}_u Du_0), \quad (\text{A3b})$$

$$A_1(z) = 2ikb_0\Lambda\mathcal{U}_\Omega a_0\rho_0(f - \mathcal{U}_\Omega\mathcal{U}_u u_0), \quad (\text{A3c})$$

$$A_0(z) = k^4b_0^4\Lambda^2\mathcal{P}\alpha + k^2b_0^2\Lambda(\Lambda a_0^2 H_B^{-1}(f - \mathcal{U}_\Omega\mathcal{U}_u u_0) + \mathcal{P}\alpha\mathcal{U}_\Omega\mathcal{U}_u\rho_0 Du_0), \quad (\text{A3d})$$

where all the basic-state functions and scale heights depend only on  $z$ . Using Expressions (19), (21), (28), and (33), the coefficients  $A_2$  and  $A_0$  may be cast in the following form:

$$A_2(z) = A_4(z)\frac{k^2b_0^2\Lambda}{\rho_0}\left(1 + \frac{\mathcal{P}\alpha\rho_0}{F}\right) - A_4(z)\left[\sigma_{\text{MRI}}^2 - \kappa^2\right], \quad (\text{A4})$$

$$A_0(z) = -A_4(z)\left(\frac{\mathcal{P}\alpha\rho_0}{F}\right)\sigma_{\text{MRI}}^2\left[\sigma_{\text{MRI}}^2 + \kappa^2\right] - A_4(z)\left(\frac{\mathcal{P}\alpha\rho_0}{F}\right)\frac{k^2b_0^2\Lambda}{\rho_0}\left[2\sigma_{\text{MRI}}^2 + \sigma_{\text{MBI}}^2\right] + \frac{A_1^2(z)}{4\mathcal{U}_\Omega^2 A_4(z)}. \quad (\text{A5})$$

## Appendix B The MRI in the Limit of a Weak Magnetic Field

In this appendix, we briefly demonstrate the relevance of assumption (16)—namely that  $1 \ll k \sim b_0^{-1}$ —by considering a simplified system in which the toroidal magnetic field is absent, i.e.,  $a_0(z) = 0$ ; in such a system, only the MRI and CI can operate (see Section 3.2). In this case, the coefficients (A1a–c) take the following form:

$$\widetilde{W}_2(z; a_0 = 0) = -k^2b_0^4(\mathcal{P}\alpha\Lambda^2) - b_0^2(2\mathcal{P}\alpha\Lambda\rho_0) - b_0^4(\Lambda^2) - k^{-2}b_0^2\sigma^4(\Lambda\rho_0) - k^{-2}\sigma^4(\rho_0^2), \quad (\text{B1})$$

$$\widetilde{W}_1(z; a_0 = 0) = b_0^2\sigma^2(\Lambda\rho_0(f - \mathcal{U}_\Omega\mathcal{U}_u u_0)) + k^{-2}\sigma^4(\rho_0^2(f - \mathcal{U}_\Omega\mathcal{U}_u u_0)), \quad (\text{B2})$$

$$\begin{aligned} \widetilde{W}_0(z; a_0 = 0) &= k^4b_0^4(\mathcal{P}\alpha\Lambda^2) + k^2b_0^2(\mathcal{P}\alpha\Lambda\rho_0(2\sigma^2 + \mathcal{U}_\Omega\mathcal{U}_u Du_0)) \\ &\quad + (\mathcal{P}\alpha\rho_0^2\sigma^2(\sigma^2 + \mathcal{U}_\Omega(\mathcal{U}_\Omega + \mathcal{U}_u Du_0))) \\ &\quad + k^2b_0^4\sigma^2((\Lambda^2) + b_0^2\sigma^4(2\Lambda\rho_0) + k^{-2}\sigma^4\rho_0^2(\sigma^2 + \mathcal{U}_\Omega^2)). \end{aligned} \quad (\text{B3})$$

The governing differential equation (14), with the coefficients defined as above, can then be considered under three asymptotic limits, keeping in mind the assumption of a weak constant poloidal magnetic field  $b_0 \rightarrow 0$ . First, for long waves, with  $k \rightarrow 0$ , it can be seen that the leading order forms of the coefficients (B1)–(B3) do not contain the magnetic field  $b_0$ , and hence the MRI does not appear at leading order. Second, for wavelengths of the order of the fluid layer thickness, namely  $k \sim 1$ , the situation is similar, but the pure CI appears at leading order. Third, the MRI can appear at leading order only for short waves, with  $k \rightarrow +\infty$ .

Having established that the relevant limits are  $b_0 \rightarrow 0$  and  $k \rightarrow +\infty$ , we can now make the relation between  $k$  and  $b_0$  more precise. To this end, in the next step of the leading order asymptotic analysis, we have to consider all possible cases that may arise from balancing different terms in the coefficients (B1)–(B3), corresponding to different relations between the parameters  $k$  and  $b_0$ . This is

similar to the procedure conducted by Gradzki & Mizerski (2018), where, in a system unstable with respect to the MBI, the weak magnetic and thermal diffusivity play a similar role to that played here by the weak magnetic field  $b_0$ , namely in establishing the wavelength of the most unstable perturbation. All three of the above orderings lead to a similar structure of the leading order equation for  $\tilde{w}_0(z)$ , with the term involving the highest order derivative multiplied by the small parameter  $k^{-2}$ . This is similar to the form of the corresponding equation in the pure MBI problem analyzed by Mizerski et al. (2013); consequently, the equations can be solved by the same boundary layer approach. It is straightforward to show, by consideration of the leading order components of the coefficients (B1)–(B3), that the regime  $k \ll b_0^{-1}$  can excite only the localized CI modes, while the regime  $b_0^{-1} \ll k$  leads to a trivial null solution. Therefore, only the relation  $k \sim b_0^{-1}$  can lead to excitation of the MRI at leading order, possibly coupled to the CI.

Hence, under the ordering (16), the growth rate at leading order,  $\sigma_0$ , can be obtained, as described in Section 3, from the equation  $\tilde{W}_0(\sigma_0, z_0; a_0 = 0) = 0$ , for a given evaluation point  $z_0$ . From Expression (B3), this equation takes the following form:

$$\sigma_0^4 + 2\sigma_0^2 \left[ \frac{k^2 b_0^2}{\rho_0(z_0)/\Lambda} + \frac{\kappa^2(z_0)}{2} \right] + \frac{k^2 b_0^2}{\rho_0(z_0)/\Lambda} \left[ \frac{k^2 b_0^2}{\rho_0(z_0)/\Lambda} + (\kappa^2(z_0) - \mathcal{U}_\Omega^2) \right] = 0, \quad (\text{B4})$$

with solutions

$$\sigma_{0\pm}^2 = -\frac{k^2 b_0^2}{\rho_0(z_0)/\Lambda} - \frac{\kappa^2(z_0)}{2} \pm \left[ \mathcal{U}_\Omega^2 \frac{k^2 b_0^2}{\rho_0(z_0)/\Lambda} + \left( \frac{\kappa^2(z_0)}{2} \right)^2 \right]^{1/2}. \quad (\text{B5})$$

In Expression (21), we choose the solution  $\sigma_{0+}^2$ , which is always greater than  $\sigma_{0-}^2$ , and denote it by  $\sigma_{\text{MRI}}^2$ .

### Appendix C Details of the Leading Order Asymptotic Analysis

Here we explore the details of the leading order asymptotic analysis of Equation (14), the general second-order ordinary differential equation for the  $z$ -dependent amplitude of the vertical velocity perturbation  $\tilde{w}(z)$ , in which the growth rate  $\sigma$  is determined as the eigenvalue of the problem. We utilize the asymptotic Rayleigh–Schrödinger approach (a type of boundary layer method), described in detail in Griffiths (2008) and used in related problems by Mizerski et al. (2013), Bowker (2016), and Gradzki & Mizerski (2018) (see also Bender & Orszag 1999).

First we consider the main flow (MF), namely the region outside the boundary layer, where the terms containing derivatives of  $\tilde{w}(z)$  in Equation (14) are not large enough to enter the leading order balance. Under the ordering (16), namely  $k \rightarrow +\infty$  and  $k \sim b_0^{-1}$ , Equation (14) at leading order takes the form

$$0 = \left[ \tilde{W}_0(z) \right] \tilde{w}_{\text{MF}}(z), \quad (\text{C1})$$

where  $\tilde{W}_0(z)$  is defined in Equation (A1c).

Since, in general,  $\tilde{W}_0(z) \neq 0$  on the domain, the only solution of Equation (C1) that satisfies at least one of the boundary conditions (15) is the null solution  $\tilde{w}_{\text{MF}}(z) = 0$ . Thus, the eigenmodes of the full problem defined by Equation (14) must involve boundary (or internal) layers, in which the derivatives of  $\tilde{w}(z)$  are sufficiently large so as to bring the second-order derivative term into play, despite its coefficient being  $O(k^{-2})$ . We thus seek nonzero solutions localized around some initially unknown point of the domain  $z_0$  ( $0 \leq z_0 \leq 1$ )—what we shall refer to as the *evaluation point*. We introduce the boundary and/or internal layer local variable  $\xi_i = (z - z_0)/\delta_i$ , where  $\delta_i$  is small—with its magnitude to be determined—and expand the growth rate as  $\sigma = \sigma_0 + \sigma_1 \delta_i + \sigma_2 \delta_i^2 + \dots$ . The solution  $\tilde{w}(z)$  and all the  $z$ -dependent basic-state functions are also evaluated in the  $\delta_i$ -vicinity of  $z_0$ . The first step is to find the leading order approximation of the growth rate, namely  $\sigma_0$ , which is presented in this section. The second step (presented in Appendix D) is to determine the higher-order correction for  $\sigma_0$ , which allows us to determine the structure of the function  $\tilde{w}_0(z)$ , the leading order asymptotic approximation of the eigenmode.

Within the boundary and/or internal layer region, Equation (14) takes the form

$$\left( \frac{\tilde{W}_2(\xi_i)}{\delta_i^2} \right) \frac{d^2 \tilde{w}_0(\xi_i)}{d\xi_i^2} + \left( \frac{\tilde{W}_1(\xi_i)}{\delta_i} \right) \frac{d\tilde{w}_0(\xi_i)}{d\xi_i} + \tilde{W}_0(\xi_i) \tilde{w}_0(\xi_i) = 0, \quad (\text{C2})$$

with transformed boundary conditions

$$\tilde{w}_0(\xi_i = -z_0/\delta_i) = \tilde{w}_0(\xi_i = (1 - z_0)/\delta_i) = 0, \quad (\text{C3})$$

where the functions  $\tilde{W}_2(z) \sim \mathcal{O}(k^{-2})$ ,  $\tilde{W}_1(z) \sim \mathcal{O}(k^{-2})$ , and  $\tilde{W}_0(z) \sim \mathcal{O}(1)$  are defined by Expressions (A1a–c). In terms of the local variable  $\xi_i$ ,  $\tilde{W}_0(\xi_i)$  may be expressed as the Taylor series

$$\tilde{W}_0(\xi_i) = \tilde{W}_0(z_0) + (\delta_i \xi_i) \left. \frac{d\tilde{W}_0(z)}{dz} \right|_{z=z_0} + \frac{(\delta_i \xi_i)^2}{2} \left. \frac{d^2\tilde{W}_0(z)}{dz^2} \right|_{z=z_0} + \dots, \quad (\text{C4})$$

with similar expansions for  $\tilde{W}_1(\xi_i)$  and  $\tilde{W}_2(\xi_i)$ .

On defining the variable  $\xi_0 = (z - z_0)/\delta_0$ , where  $\delta_0 \sim k^{-1}$  denotes the thin extent of the boundary and/or internal layer, Equation (C2) at leading order yields

$$\left( \frac{W_2(z_0)}{\delta_0^2 k^2} \right) \frac{d^2 \tilde{w}_0(\xi_0)}{d\xi_0^2} + \left( \frac{W_1(z_0)}{\delta_0 k^2} \right) \frac{d \tilde{w}_0(\xi_0)}{d\xi_0} + W_0(z_0) \tilde{w}_0(\xi_0) = 0, \quad (\text{C5})$$

where  $W_0(z_0)$ ,  $W_1(z_0)$ , and  $W_2(z_0)$ —without the tildes—denote the leading order forms at  $z_0$  of  $\tilde{W}_0(z_0)$ ,  $\tilde{W}_1(z_0)$ , and  $\tilde{W}_2(z_0)$  respectively. There are no solutions of Equation (C5) that match smoothly to the MF (zero flow) solution, and so, on this very small scale, we must require  $\tilde{w}_0(\xi_0) = \text{const.}$ , with  $W_0(z_0) = 0$ . Thus, at this order, we can deduce the form of the equation governing the leading order contribution to the growth rate. At the next order, which we discuss in Appendix D, we can establish the evaluation point  $z_0$ , which allows us to determine  $\sigma_0$ , together with the next-order correction to the growth rate,  $\sigma_1$  or  $\sigma_2$ , and also the form of the eigenfunction.

Equation (A2c) yields a quartic equation for the leading order approximation of the growth rate  $\sigma_0$  in the form

$$W_0(z_0, \sigma_0) = A_4(z_0)\sigma_0^4 + A_2(z_0)\sigma_0^2 + A_1(z_0)\sigma_0 + A_0(z_0) = 0, \quad (\text{C6})$$

where it should be noted that the coefficient  $A_1$ , defined in Equation (A3c), is purely imaginary, and thus  $\sigma_0$  is, in general, complex, even for real  $z_0$ . In the following, it is helpful to treat  $W_0$  as a function of two variables:  $W_0(z, \sigma)$ . Hence, Equation (C6) expresses the relation  $W_0(z, \sigma) = 0$  taken at an as-yet-undetermined point  $(z_0, \sigma_0)$ . It is an algebraic equation for two unknowns: the evaluation point  $z_0$  and the growth rate at leading order,  $\sigma_0$ .

The equation  $W_0(z, \sigma) = 0$  can be considered as an implicit definition of a function  $\sigma(z)$ —the so-called “growth rate function”—which can be interpreted as a “depth-dependent dispersion relation” (see Gilman 1970; Mizerski et al. 2013). It needs to be formally established by the asymptotic analysis, and for every eigenmode  $\tilde{w}(z)$  characterized by the evaluation point  $z_0$ , that the associated growth rate  $\sigma \approx \sigma(z_0)$  is the eigenvalue of the problem. The leading order approximations  $\sigma_0$  of all possible eigenvalues are considered as values of the growth rate function  $\sigma(z)$  evaluated at some (initially unknown, but determined by the analysis below) evaluation points  $z_0$ :  $\sigma_0 = \sigma(z_0)$ , where  $z_0 \in [0, 1]$ .

## Appendix D Details of the Higher-order Asymptotic Analysis

There are two cases to consider within the next-order analysis: modes  $\tilde{w}(z)$  localized near the domain boundaries,  $z_0 = 0$  or  $z_0 = 1$  (boundary layer-type solutions denoted as *wall modes*) and modes localized strictly inside the domain,  $0 < z_0 < 1$  (internal layer-type solutions denoted as *body modes*). To determine their structure, we must take into account higher-order terms in the asymptotic expansion of the growth rate  $\sigma$ ; thus, we write  $\sigma = \sigma_0 + \sigma_1 \delta_1 + \sigma_2 \delta_2^2 + \dots$ . In the case of the body modes, in order to determine both  $z_0$  and  $\sigma_0$ , we need one more equation in addition to Equation (C6). This is provided by the distinguished limit of Equation (C2) in the next-order analysis, which requires conditions (46). This section shows that the wall mode case is related to the correction  $\sigma_1$ , and the body mode case is related to the correction  $\sigma_2$ .

### D.1. Wall Modes

Here we assume that the evaluation point  $z_0$  is on the boundary of the domain, either at  $z_0 = 0$  or  $z_0 = 1$ . To find the structure of the leading order approximation for the most unstable mode  $\tilde{w}_0(z)$  and the first-order correction to the growth rate  $\sigma_1$ , we evaluate all the  $z$ -dependent functions from Equation (C2) in the  $\delta_1$ -vicinity of  $z_0$ , where  $\delta_1 \xrightarrow{k \rightarrow 0} 0$  is the boundary layer thickness, and where  $\sigma = \sigma_0 + \sigma_1 \delta_1$ . Thus, taking into account Equation (C6), obtained at the leading order of the analysis, namely  $W_0(z_0, \sigma_0) = 0$ , Equation (C2) in terms of the local variable  $\xi_1 = (z - z_0)/\delta_1$  takes the form

$$\frac{d^2 \tilde{w}_0(\xi_1)}{d\xi_1^2} = k^2 \delta_1^3 \left[ \sigma_1 \left( \frac{\partial_\sigma W_0}{W_2} \right) + \left( \frac{\partial_z W_0}{W_2} \right) \xi_1 \right] \tilde{w}_0(\xi_1), \quad (\text{D1})$$

where, here and below, the function  $W_2(z, \sigma)$  and the derivatives of  $W_0(z, \sigma)$  are taken at the point  $(z_0, \sigma_0)$  given by Equation (C6) for an assumed value of  $z_0 = 0$ , or  $z_0 = 1$ .

The boundary conditions (C3) take the following form, depending on the chosen point of evaluation  $z_0$  (i.e., whether we consider the top or bottom boundary layer mode):

$$z_0 = 0 \Rightarrow \tilde{w}_0(\xi_1 = 0) = \tilde{w}_0(\xi_1 = 1/\delta_1) = 0, \quad (\text{D2a})$$

$$z_0 = 1 \Rightarrow \tilde{w}_0(\xi_1 = -1/\delta_1) = \tilde{w}_0(\xi_1 = 0) = 0, \quad (\text{D2b})$$

under the assumptions  $k \rightarrow +\infty$ ,  $\delta_1 \rightarrow 0$ ,  $k \sim b_0^{-1}$ .

The distinguished limit is obtained by taking  $\delta_1 \sim k^{-2/3}$ , which transforms Equation (D1) to the Airy equation. To that end, we introduce a new variable  $s$  defined by

$$s(\xi_1) = (\Sigma_\sigma \sigma_1 + \Sigma_z \xi_1) \Sigma_z^{-2/3}, \quad (\text{D3})$$

where

$$\Sigma_\sigma = k^2 \delta_1^3 \left( \frac{\partial_\sigma W_0}{W_2} \right) \Big|_{z_0} = k^2 \delta_1^3 \tilde{\Sigma}_\sigma, \quad \Sigma_z = k^2 \delta_1^3 \left( \frac{\partial_z W_0}{W_2} \right) \Big|_{z_0} = k^2 \delta_1^3 \tilde{\Sigma}_z. \quad (\text{D4})$$

The three different roots of  $\Sigma_z^{-2/3}$  in Expression (D3) lead to three different forms of the new complex independent variable  $s$ . Application of the transformation (D3) to Equation (D1) leads to the standard form of the Airy equation,

$$\frac{d^2 \tilde{w}_0(s)}{ds^2} = s \tilde{w}_0(s). \quad (\text{D5})$$

The boundary conditions (D2a–b) are transformed to

$$\tilde{w}_0(s = \sigma_1 \Sigma_\sigma \Sigma_z^{-2/3}) = \tilde{w}_0(s = (\sigma_1 \Sigma_\sigma + \Sigma_z / \delta_1) \Sigma_z^{-2/3}) = 0 \quad \text{on } z_0 = 0, \quad (\text{D6a})$$

or

$$\tilde{w}_0(s = \sigma_1 \Sigma_\sigma \Sigma_z^{-2/3}) = \tilde{w}_0(s = (\sigma_1 \Sigma_\sigma - \Sigma_z / \delta_1) \Sigma_z^{-2/3}) = 0 \quad \text{on } z_0 = 1. \quad (\text{D6b})$$

For either choice of  $z_0$ , matching with the MF zero solution is achieved by

$$\tilde{w}_0(s = (\sigma_1 \Sigma_\sigma \pm \Sigma_z / \delta_1) \Sigma_z^{-2/3} \xrightarrow{\delta_1 \rightarrow 0} \infty) \rightarrow 0. \quad (\text{D7})$$

In Expression (D7), the path in the complex plane along which the limit  $s \rightarrow \infty$  is taken needs to be specified; it depends on the assumed evaluation point  $z_0$ , the values of the complex parameters  $\Sigma_\sigma$  and  $\Sigma_z$ , and on the choice of one of the three roots for the term  $\Sigma_z^{-2/3}$ .

The general solution of Equation (D5) is expressed as  $\tilde{w}_0(s) = C_A \text{Ai}(s) + C_B \text{Bi}(s)$ , where  $C_A$  and  $C_B$  are complex constants, and where  $\text{Ai}(s)$  and  $\text{Bi}(s)$ , which are linearly independent special functions, are respectively Airy functions of the first and second kind (Abramowitz & Stegun 1972; Bender & Orszag 1999). This general solution has to satisfy the boundary conditions (D6a) or (D6b), depending on whether we consider the top or bottom boundary layer mode. In both cases ( $z_0 = 0$  or  $z_0 = 1$ ), the matching condition (D7) restricts our choice of the Airy function and the root of the term  $\Sigma_z^{-2/3}$  to those that exhibit exponential decay as  $s \xrightarrow{\delta_1 \rightarrow 0} \infty$ . From the asymptotic expansions of the Airy functions for large argument, it can be shown that only the function  $\text{Ai}(s)$  for  $|\text{Arg}(s)| < \pi/3$  can satisfy this condition. This determines the choice of the root of the term  $\Sigma_z^{-2/3}$ , and hence the path of the limit  $s \rightarrow \infty$ . It follows that the solution of Equation (D5) is reduced to  $\tilde{w}_0(s) = \text{Ai}(s)$ , where, without loss of generality for this linear problem, we have set  $C_A = 1$ .

The boundary conditions (D6a) or (D6b) determine the growth rate correction  $\sigma_1$ , since, from

$$\text{Ai}(s = \sigma_1 \Sigma_\sigma \Sigma_z^{-2/3}) = 0, \quad (\text{D8})$$

we have

$$\sigma_1 = \chi_n \Sigma_\sigma^{-1} \Sigma_z^{2/3} = \chi_n (k^{-2/3} \delta_1^{-1}) \left( \frac{W_2}{\partial_\sigma W_0} \right) \left( \frac{\partial_z W_0}{W_2} \right)^{2/3}, \quad (\text{D9})$$

where  $k^{-2/3}\delta_1^{-1} \sim 1$ , and  $\chi_n$  is the  $n$ th zero of the Airy function,  $\text{Ai}(\chi_n) = 0$ . All the zeros of the Airy function of the first kind are purely real negative numbers; therefore, for a chosen evaluation point  $z_0 = 0$ , or  $z_0 = 1$ , the complex growth rate of the eigenmode  $\tilde{w}_0(s)$  has the form  $\sigma = \sigma_0 + \sigma_1\delta_1 + o(\delta_1)$ , where  $\delta_1 \sim k^{-2/3}$ , and where  $\sigma_1$  is given by Equation (D9).

Next, using Equation (D3), we can obtain the leading order approximation of the eigenmode  $\tilde{w}(z)$  as a function of the original variable  $z$ :

$$\tilde{w}_0(z) = \text{Ai} \left[ \chi_n + k^{2/3}(z - z_0) \left( \frac{\partial_z W_0}{W_2} \right)^{1/3} \right]. \quad (\text{D10})$$

It should be noted that the root of the term  $(\partial_z W_0/W_2)^{1/3} = \tilde{\Sigma}_z^{1/3}$  in Expression (D10) is already selected by the MF matching condition (D7), as described above. Moreover, utilizing the result (D9), we can simplify this matching condition to

$$\tilde{w}_0 \left( s = \chi_n \pm \frac{\tilde{\Sigma}_z^{1/3}}{\delta_1} s \xrightarrow{\delta_1 \rightarrow 0} \infty \right) \rightarrow 0, \quad (\text{D11})$$

where the  $+$  sign corresponds to  $z_0 = 0$ , and the  $-$  sign corresponds to  $z_0 = 1$ . It can be clearly seen that, in general, there are three paths for the limit  $s \rightarrow \infty$  in the complex plane, and that these are half-lines starting from  $\chi_n$  and extending to infinity. In the limit  $\delta_1 \rightarrow 0$ , the angle between each of the lines and the real axis is equal to  $\text{Arg}(\tilde{\Sigma}_z^{1/3})$ ; the smallest angle between two selected paths is always equal to  $2\pi/3$ . Since the condition  $|\text{Arg}(s)| < \pi/3$  has to be satisfied in order for the solutions to vanish at infinity, it follows that, in general, there is only one allowed path for the limit  $s \rightarrow \infty$ , with one corresponding root of  $\tilde{\Sigma}_z^{1/3}$ ; hence, the solution in the form (D10) typically exists. There is only one exception: when the parameter  $\tilde{\Sigma}_z^{1/3}$  has one purely real root—either negative when  $z_0 = 0$ , or positive when  $z_0 = 1$ . In such a case, the boundary condition (D11) cannot be satisfied, and there is no solution to Equation (D1) in the form (D10). The same situation was observed by Mizerski et al. (2013) for the case of the pure MBI when the growth rate function  $\sigma(z)$  was either increasing at  $z_0 = 0$ , or decreasing at  $z_0 = 1$ , i.e., the solution did not exist at the boundary where the growth rate function was not maximized. However, for the case at hand, the term  $\tilde{\Sigma}_z^{1/3}$  typically has three complex roots, and thus, for a fixed  $n$ , there is a unique solution in the form of Equation (D10).

Finally, in order to obtain the most unstable wall mode for a given evaluation point  $z_0$ , we take  $n = 1$  in Expressions (D9) and (D10), i.e., the first zero of the Airy function,  $\chi_1 \approx -2.338$ . This justifies Expressions (44) and (45).

## D.2. Body Modes

In this section, we assume that the evaluation point is inside the domain. As we will see, it turns out that  $z_0$  is complex; hence, to be specific, we assume that  $0 < \Re(z_0) < 1$ . However, at this stage, after the leading order growth rate analysis, we do not yet know which values of  $z_0$  are permissible and will lead to solutions for the leading order asymptotic approximation  $\tilde{w}_0(z)$  of the eigenmodes  $\tilde{w}(z)$ . An Airy function solution, as constructed for wall modes in Appendix D.1, does not decay exponentially on both sides of  $z_0$ . It thus follows that we must consider the next-order terms in the asymptotic expansions of the eigenvalue  $\sigma$  and all  $z$ -dependent functions. We therefore introduce a new boundary layer of thickness  $\delta_2 \xrightarrow{k \rightarrow 0} 0$ , and a new local variable  $\xi_2 = (z - z_0)/\delta_2$ . Equation (C2) becomes

$$\frac{d^2 \tilde{w}_0(\xi_2)}{d\xi_2^2} = \frac{k^2 \delta_2^2}{W_2} \left[ \delta_2 (\sigma_1 \partial_\sigma W_0 + \xi_2 \partial_z W_0) + \delta_2^2 \left( \frac{1}{2} \sigma_1^2 \partial_\sigma^2 W_0 + \sigma_2 \partial_\sigma W_0 + \sigma_1 \xi_2 \partial_{z,\sigma}^2 W_0 + \frac{1}{2} \xi_2^2 \partial_z^2 W_0 \right) \right] \tilde{w}_0(\xi_2), \quad (\text{D12})$$

where all the  $z$ -dependent functions are evaluated in the vicinity of an as-yet-undetermined evaluation point  $z_0$ . The function  $W_2$  and the derivatives of the function  $W_0$  are taken at  $(z_0, \sigma_0)$ , and the growth rate at leading order  $\sigma_0$  is obtained from Equation (C6), once the evaluation point  $0 < z_0 < 1$  is determined at a further stage of the analysis described below. The boundary conditions (C3) for Equation (D12) become

$$\tilde{w}_0(\xi_2 = -z_0/\delta_2) = \tilde{w}_0(\xi_2 = (1 - z_0)/\delta_2) = 0, \quad (\text{D13})$$

where we recall the asymptotic assumptions  $k \rightarrow +\infty$ ,  $b_0 \rightarrow 0$  and  $k \sim b_0^{-1}$ .

We seek a distinguished limit in Equation (D12) in which  $\partial_z W_0 = 0$ , and  $\sigma_1 = 0$ , thus removing the first bracketed term on the right-hand side. Equation (D12) then becomes

$$\frac{d^2 \tilde{w}_0(\xi_2)}{d\xi_2^2} = k^2 \delta_2^4 \left[ \sigma_2 \left( \frac{\partial_\sigma W_0}{W_2} \right) + \left( \frac{\partial_z^2 W_0}{2W_2} \right) \xi_2^2 \right] \tilde{w}_0(\xi_2). \quad (\text{D14})$$

Equation (C6), namely  $W_0(z_0, \sigma_0) = 0$ , together with the condition  $\partial_z W_0 = 0$ , now establishes the following system of two complex algebraic equations for the growth rate  $\sigma_0$  and the evaluation point  $z_0$ :

$$0 = A_4(z_0)\sigma_0^4 + A_2(z_0)\sigma_0^2 + A_1(z_0)\sigma_0 + A_0(z_0), \quad (\text{D15a})$$

$$0 = (DA_4|_{z=z_0})\sigma_0^4 + (DA_2|_{z=z_0})\sigma_0^2 + (DA_1|_{z=z_0})\sigma_0 + (DA_0|_{z=z_0}), \quad (\text{D15b})$$

where the functions  $A_i(z)$  are defined in Equations (A3a–d). The system of Equations (D15a–b) has solutions in the form of complex pairs  $(z_0, \sigma_0)$ , with the evaluation points in the form  $z_0 = \Re(z_0) + i\Im(z_0)$ , where  $0 < \Re(z_0) < 1$ . Equation (D14) must be solved for  $\delta_2 \sim k^{-1/2}$  and any pair  $(z_0, \sigma_0)$  satisfying the system of Equations (D15a–b). As in Mizerski et al. (2013), we seek to transform Equation (D14) into the form of a parabolic cylinder equation. To this end, we introduce a new variable  $\varsigma$  defined by

$$\varsigma(\xi_2) = \Upsilon_z^{1/4} \xi_2, \quad (\text{D16})$$

where

$$\Upsilon_z = k^2 \delta_2^4 \left( 2 \frac{\partial_z^2 W_0}{W_2} \right) \Bigg|_{z_0} = k^2 \delta_2^4 \tilde{\Upsilon}_z, \quad \text{say.} \quad (\text{D17})$$

The four different roots of  $\Upsilon_z^{1/4}$  in Expression (D16) lead to four different possible definitions of the new complex independent variable  $\varsigma$ . After application of the transformation of Equation (D16), Equation (D14) takes the standard form of the parabolic cylinder equation (e.g., Abramowitz & Stegun 1972; Bender & Orszag 1999):

$$\frac{d^2 \tilde{w}_0(\varsigma)}{d\varsigma^2} = \left[ \frac{1}{4} \varsigma^2 - \nu - \frac{1}{2} \right] \tilde{w}_0(\varsigma), \quad (\text{D18})$$

where the parameter  $\nu$  is defined as

$$\nu = -\frac{1}{2} - \Upsilon_\sigma \Upsilon_z^{-1/2} \sigma_2, \quad (\text{D19})$$

and with

$$\Upsilon_\sigma = k^2 \delta_2^4 \left( \frac{\partial_\sigma W_0}{W_2} \right) \Bigg|_{z_0} = k^2 \delta_2^4 \tilde{\Upsilon}_\sigma, \quad \text{say.} \quad (\text{D19})$$

The boundary conditions (D13) are now

$$\tilde{w}_0 \left( \varsigma = -z_0 \Upsilon_z^{1/4} / \delta_2 \xrightarrow{\delta_2 \rightarrow 0} \infty \right) \rightarrow 0, \quad (\text{D20a})$$

$$\tilde{w}_0 \left( \varsigma = (1 - z_0) \Upsilon_z^{1/4} / \delta_2 \xrightarrow{\delta_2 \rightarrow 0} \infty \right) \rightarrow 0, \quad (\text{D20b})$$

and where we bear in mind that there are, in general, four possible paths in the complex plane for the limit  $\varsigma \rightarrow \infty$ . The paths depend on the value of the complex evaluation point  $z_0$  as well as on the choice of the root of  $\Upsilon_z^{1/4}$ . Because we have two boundary conditions and four possible roots, we must investigate four pairs of paths.

In the case of pure MBI considered by Mizerski et al. (2013), there always exist purely real roots of  $\Upsilon_z^{1/4}$ , and furthermore,  $z_0$  is a purely real number; hence, the paths in (D20a–b) are simply the limits to real positive and negative infinity. However, for complex  $z_0$  and complex roots of  $\Upsilon_z^{1/4}$ , the pairs of paths for the limits (D20a–b) are two separate half-lines tending to infinity in directions defined by  $\text{Arg}(-z_0 \Upsilon_z^{1/4})$  and  $\text{Arg}((1 - z_0) \Upsilon_z^{1/4})$  in the limit  $\delta_2 \rightarrow 0$ . The angle between the two lines tends to  $|\text{Arg}(-z_0) - \text{Arg}(1 - z_0)|$ , which tends to  $\pi$  when  $\Im(z_0) \rightarrow 0$  and which tends to 0 when  $\Im(z_0) \rightarrow \pm\infty$ . Hence, this angle can take any value in the interval  $[0, \pi]$ , and a pair of paths for the limits (D20a–b) can, in general, have any direction in the complex plane, thus representing an important difference to the case of the pure MBI. Moreover, in the limit  $\delta_2 \rightarrow 0$ , these four pairs of paths are rotated (around the origin) relative to each other through multiples of the angle  $\pi/2$ , since they are associated with an arithmetic root of the fourth degree. This is an important property in the context of seeking solutions  $\tilde{w}_0(\varsigma)$  that satisfy the boundary conditions (D20a–b).

Solutions of Equation (D18) are known as parabolic cylinder functions; they are denoted by  $D_\nu(\pm \varsigma)$  and  $D_{-\nu-1}(\pm i\varsigma)$ , where only two of these functions are linearly independent. To obtain the solution that satisfies the boundary conditions (D20a–b), we first need to find the regions in the complex plane where the parabolic cylinder functions decay to zero or diverge to infinity as  $\varsigma \rightarrow \infty$ . From the asymptotic expansions of the parabolic cylinder functions in the limit  $\varsigma \rightarrow \infty$ , it can be shown that

1.  $|\text{Arg}(\varsigma)| < \frac{1}{4}\pi \Rightarrow D_\nu(\pm\varsigma) \xrightarrow{\varsigma \rightarrow \infty} 0$  and  $D_{-\nu-1}(\pm i\varsigma) \xrightarrow{\varsigma \rightarrow \infty} \infty$  for all values of  $\nu$ ;
2.  $\frac{3}{4}\pi < \text{Arg}(\varsigma) < \frac{5}{4}\pi \Rightarrow D_\nu(\pm\varsigma) \xrightarrow{\varsigma \rightarrow \infty} 0$  only for the values of  $\nu$  such that  $1/\Gamma(-\nu) = 0$ ; also  $D_{-\nu-1}(\pm i\varsigma) \xrightarrow{\varsigma \rightarrow \infty} \infty$  for all values of  $\nu$ ;
3.  $\left(\frac{1}{4}\pi < \text{Arg}(\varsigma) < \frac{3}{4}\pi\right) \cup \left(\frac{5}{4}\pi < \text{Arg}(\varsigma) < \frac{7}{4}\pi\right) \Rightarrow D_{-\nu-1}(\pm i\varsigma) \xrightarrow{\varsigma \rightarrow \infty} 0$  and  $D_\nu(\pm\varsigma) \xrightarrow{\varsigma \rightarrow \infty} \infty$  for all values of  $\nu$ .

It follows that the boundary conditions (D20a–b) impose the solution either in the form  $D_\nu(\pm\varsigma)$  or  $D_{-\nu-1}(\pm i\varsigma)$ , for pairs of paths along which the limits  $\varsigma \rightarrow \infty$  are taken either within region 3 defined above (for the latter case of  $D_{-\nu-1}(\pm i\varsigma)$ ) or in the sum of regions 1 and 2 (for the former case of  $D_\nu(\pm\varsigma)$ ). In general, for any pair  $(z_0, \sigma_0)$  satisfying the system (D15a–b) we may have one or more of the following situations:

- (a) For at least one pair of paths, one of the paths lies in region 3 and the other lies in regions 1 or 2.
- (b) There is a pair of paths with both paths lying in region 1 or both in region 3.
- (c) There is one pair of paths with both paths lying in region 2.
- (d) There are two pairs of paths with one path in region 1 and the other in region 2. These two pairs of paths are symmetrical about the origin.

It is straightforward to see that for case (a) there are no solutions that satisfy both boundary conditions (D20a–b) for any root of  $\Upsilon_z^{1/4}$ . Cases (b) and (c) can occur simultaneously, as well as (b) and (d), owing to the  $(\pi/2)$ -shift between the roots. However, in case (b), the relevant parabolic cylinder functions satisfy the boundary conditions for all values of the parameter  $\nu$ , which means that the correction  $\sigma_2$  related to  $\nu$  through Equation (D19) cannot be determined; hence, also the form of the solution  $\tilde{w}_0(\varsigma)$  cannot be determined at this order. We can obtain the correction  $\sigma_2$  only for cases (c) or (d), namely when there exists at least one pair of paths with at least one path in region 2; i.e., the region where some restriction on the parameter  $\nu$  is imposed. For this case, we can write down the solution in the form  $\tilde{w}_0(\varsigma) = D_\nu(\varsigma)$ . The condition  $1/\Gamma(-\nu) = 0$  determines all possible values of the parameter  $\nu$ , which must be a nonnegative integer,  $\nu = 0, 1, 2, 3, \dots$ . Hence, from Equation (D19), we obtain

$$\sigma_2 = \left(-\frac{1}{2} - \nu\right) \Upsilon_\sigma^{-1} \Upsilon_z^{1/2} = \left(-\frac{1}{2} - \nu\right) k^{-1} \delta_2^{-2} \left(\frac{W_2}{\partial_\sigma W_0}\right) \left(2 \frac{\partial_z^2 W_0}{W_2}\right)^{1/2}, \quad (\text{D21})$$

where  $k^{-1} \delta_2^{-2} \sim 1$ . We note that, in Expression (D21),  $\Upsilon_z$  appears as a square root but not as a smaller power; hence, even in case (d), the value of  $\sigma_2$  is determined uniquely, even though there are two distinct roots of  $\Upsilon_z^{1/4}$  that lead to the solution. In case (c), only one root of  $\Upsilon_z^{1/4}$  is allowed.

In the case of  $\nu = 0, 1, 2, 3, \dots$ , the parabolic cylinder function  $D_\nu(x)$  can be expressed in terms of the  $\nu$ -degree modified Hermite polynomial  $\text{He}_\nu(x)$  as  $D_\nu(x) = \exp(-x^2/4) \text{He}_\nu(x)$ ; the first few polynomials  $\text{He}_\nu(x)$  are  $\text{He}_0(x) = 1$ ,  $\text{He}_1(x) = x$ ,  $\text{He}_2(x) = x^2 - 1$ ,  $\text{He}_3(x) = x^3 - 3x$  (see Abramowitz & Stegun 1972; Bender & Orszag 1999). Thus, for any pair  $(z_0, \sigma_0)$  for which there exists a solution (with a uniquely determined correction  $\sigma_2$ ) given by Equation (D21), the complex growth rate of the eigenmode  $\tilde{w}(s)$  is given by  $\sigma = \sigma_0 + \sigma_2 \delta_2^2 + o(\delta_2^2)$ , where  $\delta_2 \sim k^{-1/2}$ . The leading order approximation of such an eigenmode, expressed as a function of the original independent variable  $z$ , takes the form

$$\tilde{w}_0(z) = \exp\left[-\frac{1}{4}k(z - z_0)^2 \left(2 \frac{\partial_z^2 W_0}{W_2}\right)^{1/2}\right] \text{He}_\nu\left[k^{1/2}(z - z_0) \left(2 \frac{\partial_z^2 W_0}{W_2}\right)^{1/4}\right], \quad (\text{D22})$$

where  $z_0$  is the complex evaluation point, with the real part satisfying  $0 < \Re(z_0) < 1$ .

Finally, the most unstable body mode for a given evaluation point  $z_0$  is defined by  $\nu = 0$ , i.e., the smallest possible value of the parameter  $\nu$  in Expressions (D21) and (D22). This justifies Expressions (48) and (50); the former, in particular, is relatively simple, since  $\text{He}_0(x) = 1$ . This allows us readily to determine the localization point  $z_{\text{max}}$  (different from the evaluation point  $z_0$ ) of the Gaussian-shaped function modulus  $|\tilde{w}_0(z)|$  for  $\nu = 0$ . The resulting expression for  $z_{\text{max}}$  is given by Equation (49).

## ORCID iDs

M. J. Gradzki  <https://orcid.org/0000-0002-5115-251X>  
 D. W. Hughes  <https://orcid.org/0000-0002-8004-8631>  
 K. A. Mizerski  <https://orcid.org/0000-0003-0106-675X>

## References

- Abramowitz, M., & Stegun, I. A. 1972, *Handbook of Mathematical Functions* (New York: Dover)
- Acheson, D. J. 1978, *RSPTA*, **289**, 459
- Acheson, D. J. 1979, *SoPh*, **62**, 23
- Balbus, S. A. 2003, *ARA&A*, **41**, 555
- Balbus, S. A., & Hawley, J. F. 1991, *ApJ*, **376**, 214
- Balbus, S. A., & Hawley, J. F. 1998, *RvMP*, **70**, 1
- Bender, C. M., & Orszag, S. A. 1999, *Advanced Mathematical Methods for Scientists and Engineers* (New York: Springer)
- Bowker, J. A. 2016, PhD thesis, Univ. Leeds
- Brandenburg, A., & Schmitt, D. 1998, *A&A*, **338**, L55
- Cattaneo, F., Chiueh, T., & Hughes, D. W. 1990, *JFM*, **219**, 1
- Cattaneo, F., & Hughes, D. W. 1988, *JFM*, **196**, 323
- Chandrasekhar, S. 1960, *PNAS*, **46**, 253
- Chatterjee, P., Mitra, D., Rheinhardt, M., & Brandenburg, A. 2011, *A&A*, **534**, A46
- Fan, Y. 2001, *ApJ*, **546**, 509
- Foglizzo, T., & Tagger, M. 1994, *A&A*, **287**, 297
- Forgács-Dajka, E., & Petrovay, K. 2002, *A&A*, **389**, 629
- Fromang, S., Latter, H., Lesur, G., & Ogilvie, G. I. 2013, *A&A*, **552**, A71
- Gilman, P. A. 1970, *ApJ*, **162**, 1019
- Gilman, P. A. 2018a, *ApJ*, **853**, 65
- Gilman, P. A. 2018b, *ApJ*, **867**, 45
- Goodman, J., & Ji, H. 2002, *JFM*, **462**, 365
- Gough, D. O. 2007, in *The Solar Tachocline*, ed. D. W. Hughes, R. Rosner, & N. O. Weiss (New York: Cambridge Univ. Press), 3
- Gradzki, M. J., & Mizerski, K. A. 2018, *ApJS*, **235**, 13
- Griffiths, S. D. 2008, *JFM*, **605**, 115
- Hawley, J. F., Gammie, C. F., & Balbus, S. A. 1995, *ApJ*, **440**, 742
- Hollerbach, R., & Rüdiger, G. 2005, *PhRvL*, **95**, 124501
- Hughes, D. W. 1985, *GApFD*, **32**, 273
- Hughes, D. W. 2007, in *The Solar Tachocline*, ed. D. W. Hughes, R. Rosner, & N. O. Weiss (Cambridge: Cambridge Univ. Press), 275
- Hughes, D. W., & Brummell, N. H. 2021, *ApJ*, **922**, 195
- 2007, in *The Solar Tachocline*, Hughes, D. W., Rosner, R., & Weiss, N. O. (ed.) (Cambridge: Cambridge Univ. Press)
- Jones, C. A., Soward, A. M., & Mussa, A. I. 2000, *JFM*, **405**, 157
- Kersalé, E., Hughes, D. W., & Tobias, S. M. 2007, *ApJL*, **663**, L113
- Kim, J., Hong, S. S., Ryu, D., & Jones, T. W. 1998, *ApJL*, **506**, L139
- Matthews, P. C., Hughes, D. W., & Proctor, M. R. E. 1995, *ApJ*, **448**, 938
- Mizerski, K. A., Davies, C. R., & Hughes, D. W. 2013, *ApJS*, **205**, 16
- Newcomb, W. A. 1961, *PhFl*, **4**, 391
- Ogilvie, G. I. 2007, in *The Solar Tachocline*, ed. D. W. Hughes, R. Rosner, & N. O. Weiss (Cambridge: Cambridge Univ. Press), 299
- Parker, E. N. 1966, *ApJ*, **145**, 811
- Rayleigh, L. 1917, *RSPSA*, **93**, 148
- Shampine, L. F., & Kierzenka, J. 2001, *ACM Trans. Math. Softw.*, **27**, 299
- Silvers, L. J., Vasil, G. M., Brummell, N. H., & Proctor, M. R. E. 2009, *ApJL*, **702**, L14
- Soward, A. M. 1977, *GApFD*, **9**, 19
- Soward, A. M., & Jones, C. A. 1983, *QJMAM*, **36**, 19
- Vasil, G. M., & Brummell, N. H. 2008, *ApJ*, **686**, 709
- Velikhov, E. P. 1959, *Sov. Phys. JETP*, **36**, 1398
- Wissink, J. G., Hughes, D. W., Matthews, P. C., & Proctor, M. R. E. 2000, *MNRAS*, **318**, 501
- Yano, J.-I. 1992, *JFM*, **243**, 103